

# Interacting dark energy from the joint analysis of the power spectrum and bispectrum multipoles with the EFTofLSS

Maria Tsedrik,<sup>1</sup> Chiara Moretti,<sup>1,2,5</sup> Pedro Carrilho,<sup>1</sup> Federico Rizzo,<sup>2,3,4</sup> Alkistis Pourtsidou<sup>1,5</sup>

<sup>1</sup>*Institute for Astronomy, The University of Edinburgh, Royal Observatory, Edinburgh EH9 3HJ, UK*

<sup>2</sup>*Istituto Nazionale di Astrofisica, Osservatorio Astronomico di Trieste, via Tiepolo 11, 34143 Trieste, Italy*

<sup>3</sup>*Istituto Nazionale di Fisica Nucleare, Sezione di Trieste, via Valerio 2, 34127 Trieste, Italy*

<sup>4</sup>*Institute for Fundamental Physics of the Universe, Via Beirut 2, 34151 Trieste, Italy*

<sup>5</sup>*Higgs Centre for Theoretical Physics, School of Physics and Astronomy, The University of Edinburgh, Edinburgh EH9 3FD, UK*

Accepted XXX. Received YYY; in original form ZZZ

## ABSTRACT

Interacting dark energy models have been suggested as alternatives to the standard cosmological model,  $\Lambda$ CDM. We focus on a phenomenologically interesting class of dark scattering models that is characterised by pure momentum exchange between dark energy and dark matter. This model extends the parameter space with respect to  $\Lambda$ CDM by two parameters,  $w$  and  $A$ , which define the dark energy equation of state and the strength of the coupling between dark energy and dark matter, respectively. In order to test non-standard cosmologies with Stage-IV galaxy clustering surveys, it is crucial to model mildly nonlinear scales and perform precision vs accuracy tests. We use the Effective Field Theory of Large-Scale Structure, and we perform validation tests by means of an MCMC analysis using a large set of N-body simulations. We find that adding the bispectrum monopole to the power spectrum multipoles improves the constraints on the dark energy parameters by  $\sim 30\%$  for  $k_{\max, B}^{l=0} = 0.11 h \text{ Mpc}^{-1}$  without introducing biases in the parameter estimation. We also find that the same improvement can be achieved with more moderate scale cuts and the use of bias relations, or with the addition of the bispectrum quadrupole. Finally, we forecast constraints assuming Stage-IV surveys specifications at  $z = 1$  in the interacting dark energy scenario:  $\sigma_w = 0.08$  and  $\sigma_A = 2.51 \text{ b GeV}^{-1}$ , as well as for  $w$ CDM cosmology:  $\sigma_w = 0.1$ .

**Key words:** cosmology: large-scale structure of Universe – cosmology: cosmological parameters – cosmology: dark energy

## 1 INTRODUCTION

In the next few years, Stage-IV galaxy surveys such as the Dark Energy Survey (DES)<sup>1</sup> (Abbott et al. 2021), the Dark Energy Spectroscopic Instrument (DESI)<sup>2</sup> (Aghamousa et al. 2016), Euclid<sup>3</sup> (Lau-reijss et al. 2011), the Nancy Grace Roman Space Telescope<sup>4</sup> (Spergel et al. 2015), and the Vera C. Rubin Observatory’s Legacy Survey of Space and Time (LSST)<sup>5</sup> (Ivezic et al. 2019) promise to provide high precision measurements, which will allow us to study the large-scale structure of the Universe with unprecedented accuracy. A key goal of these surveys is to test for deviations from the standard cosmological model,  $\Lambda$ CDM. The  $\Lambda$ CDM model postulates two exotic components: cold dark matter (CDM), and dark energy in the form of a cosmological constant ( $\Lambda$ ). The nature of these dark sector components is unknown. Moreover, in recent years issues related to tensions in the determination of the  $H_0$  and  $\sigma_8$  cosmological parameters between early and late Universe probes have emerged. The search for alternatives to  $\Lambda$ CDM that could also explain the apparent tensions

has led to a plethora of exotic dark energy, dark matter, and modified gravity theories (for reviews see Copeland et al. 2006; Bertone et al. 2005; Clifton et al. 2012; Perivolaropoulos & Skara 2021). In preparation for the stringent tests of these theories with forthcoming data, validation tests of the exotic models against simulations have to be performed. One of these non-standard cosmological models, called Interacting Dark Energy, is the focus of this study.

The term Interacting Dark Energy (IDE) describes a broad class of models, in which a non-gravitational coupling between dark energy and dark matter is allowed. A large suite of such models can be constructed by making different choices for the form of the coupling function (for instance, Amendola 2000; Farrar & Peebles 2004; Clemson et al. 2012; Pourtsidou et al. 2013). Interacting dark energy models have also been considered as candidate models to alleviate the  $\sigma_8$  and  $H_0$  tension, with various degrees of success (Pourtsidou & Tram 2016; Baldi & Simpson 2017; Barros et al. 2019; Di Valentino et al. 2020a,b; Kase & Tsujikawa 2020; Amendola & Tsujikawa 2020; Beltrán Jiménez et al. 2021). The vast majority of models exhibits background energy transfer. As a result, they are severely constrained by Cosmic Microwave Background (CMB), Baryonic Acoustic Oscillations (BAO) and Supernovae (SNeIa) measurements (for instance, Xia 2009; Di Valentino et al. 2017; van de Bruck & Thomas 2019; Pan et al. 2019; Gómez-Valent et al. 2020; Yang et al. 2021; Nunes et al. 2022). In this work we consider a popular class of IDE models, which is uncoupled in the background and exhibits

\* E-mail: mtsedrik@ed.ac.uk

<sup>1</sup> <https://www.darkenergysurvey.org/>

<sup>2</sup> <https://www.desi.lbl.gov/>

<sup>3</sup> <http://euclid-ec.org>

<sup>4</sup> <https://www.nasa.gov/roman>

<sup>5</sup> <https://www.lsst.org/>

only momentum exchange between dark energy and dark matter, at the level of the linear perturbations. This feature makes the model capable of fitting both large-scale structure (LSS) and CMB measurements extremely well for a wide range of couplings (Poulsidou & Tram 2016; Baldi & Simpson 2017; Spurio Mancini & Poulsidou 2022).

In contrast to modified gravity (MG) theories, IDE models do not influence the speed of gravitational waves or the gravitational potential of planets, hence they do not need screening mechanisms in order to surpass Solar System tests. Furthermore, instead of an enhancement in the growth of structure at nonlinear scales (as in the case of popular MG models, e.g., Sotiriou & Faraoni 2010), some interacting models predict a suppression of growth and hence lead to an alleviation of the  $\sigma_8$  tension.

Non-standard cosmologies generally have a larger parameter space (more free parameters) than  $\Lambda$ CDM, and these may result to observable effects at linear and nonlinear scales. For example, Baldi & Simpson (2015) showed that nonlinear scales are much more informative in terms of constraints for dark matter - dark energy scattering than the linear regime. This highlights the importance of accurately modelling nonlinear scales for extended models. The specific IDE model under consideration in this work was studied by Carrilho et al. (2021). The authors used a set of approximate (COLA) simulations run with standard cosmology to perform null tests of three perturbative approaches to compute the halo power spectrum multipoles. The authors conclude that a) a false  $\sim 3\sigma$  detection of exotic dark energy would occur should the nonlinear modelling be incorrect b) precise and accurate constraints on IDE parameters are possible when appropriate scale cuts are considered, and c) the Effective Field Theory of Large-Scale Structure (EFTofLSS) approach (Baumann et al. 2012; Carrasco et al. 2012; d'Amico et al. 2020; Rizzo et al. 2022) provides a model accurate up to a wave-number of  $k_{\max} \sim 0.3 h \text{ Mpc}^{-1}$ . In this study we apply the same model and extend upon the previous work by adding the bispectrum monopole and quadrupole to the analysis, and by using better simulations.

The joint analysis of the power spectrum and bispectrum has been considered for Stage-IV surveys analyses that aim to constrain  $\Lambda$ CDM. The addition of the bispectrum is useful for breaking bias degeneracies and tightly constraining bias parameters. An example is the significant increase in the constraining power on the mass fluctuation amplitude  $A_s$  when the real space analysis includes the bispectrum (Eggemeier et al. 2021): indeed, the bispectrum is able to break the strong degeneracy between  $A_s$  and the linear bias,  $b_1$ . This is however no longer the case in redshift space, since the aforementioned degeneracy is already broken at the level of the power spectrum multipoles. There are various examples of the joint analysis in redshift space in the literature. To name a few, a Fisher Matrix forecast analysis was performed in Yankelevich & Porciani (2019) with tree-level Standard Perturbation Theory (SPT) (Bernardeau et al. 2002); a full likelihood analysis was done in Gualdi & Verde (2020) and Gualdi et al. (2021) with the TNS modelling (Taruya et al. 2010) and the Quijote suite of N-body simulations (Villaescusa-Navarro et al. 2020), as well as in d'Amico et al. (2020); Philcox & Ivanov (2022); Ivanov et al. (2022), with data from the BOSS survey (Beutler et al. 2017) and the EFTofLSS model. The above forecasts and data analyses concentrated on the  $\Lambda$ CDM model. In this paper we analyse the informational content of the bispectrum in addition to the power spectrum in redshift space for a non-minimal, interacting dark energy model. To our knowledge, this is the first analysis of this kind for exotic dark energy.

This paper is organized as follows: section 2 is dedicated to the specific interacting dark energy model we use in our work, its main

features and impact on structure formation; in section 3 we describe the EFTofLSS model for the power spectrum and bispectrum with a brief overview on the nuisance parameters and their co-dependencies. In section 4 we describe our likelihood pipeline and performance metrics. Our results are presented in section 5. We conclude in section 6.

## 2 INTERACTING DARK ENERGY MODELLING

In this work we focus on the subclass of IDE models which exhibits no coupling at the background level and introduces a pure momentum transfer at the level of linear perturbations. In general, non-gravitational interaction between dark matter and dark energy can be introduced either at the level of the action (Poulsidou et al. 2013; Tamanini 2015; Kase & Tsujikawa 2020) or more phenomenologically at the level of the fluid equations (e.g., Väliviita et al. 2008; Simpson 2010). This leads to two different approaches for our model of interest.

The first approach corresponds to the “Type 3” class of models from the action-based derivation in Poulsidou et al. (2013). There, the pure exchange of momentum is generated by a coupling between the dark matter velocity field and the covariant derivative of the dark energy scalar field. In this case, the two parameters describing the extension with respect to the standard cosmological model are given by the coupling strength  $\beta$  and the exponential factor of the quintessence potential  $\lambda$ . These parameters are included in the action as follows:

$$S_\phi = \int dt d^3x a^3 \left[ \frac{1}{2}(1-2\beta)\dot{\phi}^2 - \frac{1}{2}|\nabla\phi|^2 - V_0 e^{-\lambda\phi} \right], \quad (1)$$

where  $\phi$  is the scalar field (quintessence), the last term is the quintessence potential of the single exponential form, the dot represents a derivative with respect to cosmic time and  $a$  is the scale factor. This model is explicitly studied in Poulsidou & Tram (2016), Spurio Mancini & Poulsidou (2022) and has been implemented into the CLASS (Lesgourges 2011; Blas et al. 2011) and CAMB (Lewis & Challinor 2011) Boltzmann codes. These analyses vary  $\beta$  and  $\lambda$ , while the quintessence potential normalisation,  $V_0$ , is varied automatically by the Boltzmann solver in order to match a given  $\Omega_\phi$  today.

The second approach is derived in the elastic scattering formalism by Simpson (2010). The main idea is that a dark matter particle moves through the isotropic dark energy fluid and experiences a drag-force proportional to the scattering cross-section between the particle and the fluid. Since a dark matter particle is more massive than the energy exchange with the dark energy fluid, they interact via elastic scattering, in a way that resembles Thomson scattering between non-relativistic electrons and photons in the radiation-dominated era.

Such interaction involves no energy transfer and hence it leaves the energy conservation equation unchanged with respect to the standard cosmology. Moreover, we assume that the dark energy density and velocity fields are homogeneous (i.e.  $\delta_{DE} = \theta_{DE} = 0$ ), since dark energy perturbations are damped within the cosmic horizon. This follows from the assumption of the dark energy speed of sound being equal to the speed of light, and was confirmed numerically in Baldi & Simpson (2015). While these fluctuations become non-negligible at super-horizon scales, even the most extreme modifications do not contradict the CMB measurements due to the presence of cosmic variance (Poulsidou & Tram 2016). In presence of momentum exchange between the two components of the dark sector, and with the approximation of homogeneity in dark energy, this IDE model

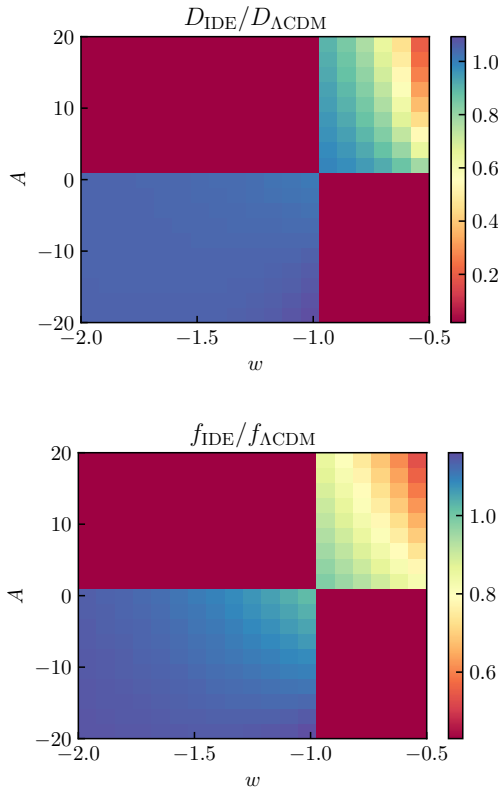


**Figure 1.** Top: the ratio of the linear growth factor to the  $\Lambda$ CDM case  $D_{\Lambda\text{CDM}} = 0.475$  for the different values of IDE parameters. Bottom: the ratio of the logarithmic growth rate to the  $\Lambda$ CDM case  $f_{\Lambda\text{CDM}} = 0.861$  for the different values of IDE parameters. Both growth parameters are computed at redshift  $z = 1$ . Parameter  $A$  is given in the units of  $\text{b GeV}^{-1}$ . The red patches in the upper left and the lower right corners denote the forbidden area of the IDE parameter space due to the condition  $A/(1+w) \geq 0$ .

modifies only the Euler equation to

$$a \partial_a \Theta + \left( 2 + (1+w) \xi \frac{\rho_{\text{DE}}}{H} + \frac{a \partial_a H}{H} \right) \Theta + \frac{\nabla^2 \Phi}{a^2 H^2} = 0, \quad (2)$$

where  $\xi = \sigma_{\text{D}}/m_{\text{c}}$  with  $\sigma_{\text{D}}$  is the cross-section of the dark energy - dark matter interaction and  $m_{\text{c}}$  the mass of dark matter particle, and  $\Theta = \theta_{\text{c}}/aH$  with  $\theta_{\text{c}}$  the dark matter velocity divergence.  $H = \dot{a}/a$  is the Hubble rate and it describes the expansion history in the flat universe composed only of dark matter and dark energy by

$$H^2 = H_0^2 \left( \Omega_{\text{c},0} a^{-3} + \Omega_{\text{DE},0} a^{-3(1+w)} \right), \quad (3)$$

where as above  $w$  is the dark energy equation of state parameter.  $H_0$ ,  $\Omega_{\text{c},0}$ ,  $\Omega_{\text{DE},0}$  are the values of Hubble parameter, dark matter density and dark energy density parameters today. Additionally, the gravitational potential stays unchanged and is given by the following Poisson equation:

$$\nabla^2 \Phi = \frac{3}{2} a^2 H^2 \Omega_{\text{c}} \delta_{\text{c}}, \quad (4)$$

where  $\Omega_{\text{c}}$  is the background dark matter density parameter at the scale factor  $a$  and  $\delta_{\text{c}}$  is the corresponding density contrast.

Although there is no direct mapping between the elastic scattering and the “Type 3” models, a particular subclass of “Type 3” models can reproduce the drag-like behaviour (Skordis et al. 2015). In Baldi & Simpson (2017) the authors show how these models can be

matched approximately. In this work we use the phenomenological approach with parameters  $w$  and  $A = \xi(1+w)$ , which characterise the equation of state for dark energy and the coupling strength, respectively. We assume that  $w$  is constant, it affects the expansion history in Equation 3 as well as structure formation in Equation 2. At the same time,  $A$  impacts only the perturbation growth and is chosen in this form (i.e. a combination of  $\xi$  and  $w$ ) for the purposes of parameter inference. This is particularly important for  $w \approx -1$ , where we can constrain  $A$  while  $\xi$  could take an arbitrary large value.

Parameters  $w$  and  $A$  modify the linear growth factor  $D(a)$  and the logarithmic growth rate  $f = d \ln D / d \ln a$ . For a constant value of  $w$  in the late Universe with redshift  $z \leq 10$ , in the canonical (phantom) case of  $w_{\text{DE}} > -1$  ( $w_{\text{DE}} < -1$ ) the growth factor is decreased (increased) with respect to  $\Lambda$ CDM. The effect gets more prominent as the redshift decreases, and for larger values of  $\xi$ . This leads to a scale-independent suppression (enhancement) of the power spectrum at large scales. On smaller scales, the modification comes from the drag term in Equation 2: for  $w_{\text{DE}} > -1$  ( $w_{\text{DE}} < -1$ ) there is a dissipation (injection) of kinetic energy within collapsed structures. In other words, for  $w_{\text{DE}} > -1$  ( $w_{\text{DE}} < -1$ ) particles inside collapsed objects experience additional friction (drag), hence it becomes harder (easier) for them to stream away, with a strong and scale-dependent enhancement (suppression) of the growth of structure in the nonlinear regime. This behaviour, anticipated from the theory, has been shown to hold true in N-body simulations by Baldi & Simpson (2015) and Baldi & Simpson (2017).

In this work we consider only one redshift  $z = 1$ , at which the impact of the IDE parameters is observable but not as prominent as at lower redshifts. In Figure 1 we show the impact of different values of  $w$  and  $A$  on the growth parameters at the redshift of our interest. The ratios are taken with respect to the  $\Lambda$ CDM values:  $D_{\Lambda\text{CDM}} = 0.475$  and  $f_{\Lambda\text{CDM}} = 0.861$  for our choice of cosmological parameters. The red patches in the upper left and the lower right corners denote the forbidden area of the IDE parameter space: the sign of  $A$  and  $(1+w)$  has to be the same, since  $\xi = A/(1+w)$  from Equation 2 has to be non-negative. For  $w < -1$  dark energy starts to dominate over matter at later times than in  $\Lambda$ CDM, hence with decreasing  $w$  the growth rate quickly becomes 1 (as in the matter-dominated epoch) nearly independent from the value of  $A$ . The linear growth factor is also independent of  $A$  and is slightly larger than the  $\Lambda$ CDM case for  $w < -1$ . For  $w > -1$  the expected power suppression at linear scales is present, with a stronger effect for larger values of  $A$ .

### 3 POWER SPECTRUM AND BISPECTRUM MODELLING

Halos and galaxies are biased tracers of the matter density field (Desjacques et al. 2018). Their clustering properties up to mildly nonlinear scales can be described using the perturbative framework. The EFTofLSS formalism is based on perturbation theory, with the addition of counterterms to account for the impact of unknown small-scale physics, such as galaxy formation, on large-scale modes. The functional form of the counterterms is specified by the symmetries of the density field, while the nuisance parameters are determined by the data. We note that application to data would not be possible without huge effort in the development on the theoretical side (see for example Bernardeau et al. 2002; Crocce & Scoccimarro 2008; Taruya et al. 2010; Senatore & Zaldarriaga 2014, 2015; Vlah et al. 2015; Baldauf et al. 2015b; Perko et al. 2016; Vlah & White 2019, and for a more comprehensive list for the development of the EFTofLSS see the footnote in D’Amico et al. 2022).

### 3.1 Bias expansion

Both dark matter halos (the focus of this study) and galaxies are biased tracers of the underlying matter distribution. The halo over-density can be expanded as  $\delta_h = \sum_n b_n / n! \delta^n$ , where  $\delta^n$  are higher powers of the matter density contrast and  $b_n$  are the corresponding local bias terms (Fry & Gaztanaga 1993). Halos are formed by the gravitational collapse of matter from a spatially finite region. Anisotropies created by this process impact the local distribution of objects, and thus the bias parameters, with tidal effects (Chan et al. 2012; Baldauf et al. 2012) and introduce scale dependency by breaking the local assumption (McDonald & Roy 2009). Effects from an ellipsoidal gravitational collapse are encoded in the non-local operators, dubbed  $\mathcal{G}_2$  and  $\Gamma_3$ : the first one represents the tidal stress tensor produced by the gravitational potential, while the second one denotes the difference between the tidal stress tensors from the gravitational and velocity potentials. Effects due to the finite size of the collapsing region are taken into account by the higher-order derivative of the matter field  $\nabla^2 \delta$ . Additionally, the relation between matter and galaxies is also affected by stochasticity, whose impact can be modeled as an additional contribution to Poisson shot noise on large scales (Seljak et al. 2009; Paech et al. 2017), while on small scales it can exhibit a scale-dependence due to the halo-exclusion effect (Baldauf et al. 2013a; Eggemeier et al. 2020). We consider the bias expansion given by (Desjacques et al. 2018; Assassi et al. 2014):

$$\delta_h = b_1 \delta + \frac{b_2}{2} \delta^2 + b_{\mathcal{G}_2} \mathcal{G}_2 + b_{\Gamma_3} \Gamma_3 + b_{\nabla^2 \delta} \nabla^2 \delta + \epsilon + \epsilon_{\delta} \delta, \quad (5)$$

where  $b_1$  and  $b_2$  are the linear and quadratic bias, and the last two terms correspond to stochasticity contributions. Note that the higher derivative term gives rise to a  $k^2 P_L(k)$  correction, which is degenerate with one of the counterterms. Therefore, we omit  $b_{\nabla^2 \delta}$  in our analysis, as previously done in Oddo et al. (2021). Moreover, we omit from Equation 5 all operators that do not contribute to our chosen theoretical models for the power spectrum and bispectrum.

### 3.2 Power spectrum and bispectrum

The mildly nonlinear power spectrum and bispectrum in real space using the EFTofLSS can be modeled with three ingredients: a) the leading-order contribution in SPT at one-loop for the power spectrum with the addition of the EFTofLSS counterterms, and at tree-level for the bispectrum, b) a bias expansion, and c) an infrared-resummation routine to take the damping of the oscillatory features into account (Baldauf et al. 2015a; Blas et al. 2016). In addition to that, to model redshift space quantities we should take the distortions due to peculiar velocities into consideration. This introduces an additional dependency of the observables on the direction of separation between the objects with respect to the line-of-sight,  $\hat{s}$ . For the power spectrum this dependency is characterized by the cosine of the angle formed by the separation wave-number with the line-of-sight,  $\mu = (\mathbf{k} \cdot \hat{s})/k$ . For the bispectrum we need two cosines,  $\mu_1$  and  $\mu_2$ , of  $\mathbf{k}_1$  and  $\mathbf{k}_2$  with the line of sight  $\hat{s}$ , with the condition  $\mathbf{k}_1 + \mathbf{k}_2 + \mathbf{k}_3 = \mathbf{0}$ . However, it is more convenient to describe triangle configurations with three wave-numbers ( $k_1, k_2, k_3$ ), and two angles,  $\theta = \arccos \mu_1$  and  $\xi$  being the azimuthal rotational angle of  $\mathbf{k}_2$  around  $\mathbf{k}_1$  (Scoccimarro et al. 1999a). In total, the redshift space bispectrum depends on five variables, three of which determine the shape of the triangle while the remaining two define its orientation with respect to the line-of-sight.

The complete set of equations we use in this work will be detailed in a forthcoming paper by Moretti et al. (2022), where we also give a detailed description of the code used to perform the analysis. Here we briefly highlight the main formulae and techniques used. These

formulae are the same as in  $\Lambda$ CDM, as the interaction under consideration only modifies the linear growth factor,  $D$  (appearing below via  $P_L$ ) and the linear growth rate of structure,  $f$ .

The expression for the halo power spectrum in redshift space that we adopt in our analysis is given by:

$$\begin{aligned} P_{hh}(k, \mu) = & Z_1(\mathbf{k}) P_L(k) \\ & + 2 \int d^3 q [Z_2(\mathbf{q}, \mathbf{k} - \mathbf{q})]^2 P_L(q) P_L(|\mathbf{k} - \mathbf{q}|) \\ & + 6 Z_1(\mathbf{k}) P_L(k) \int d^3 q Z_3(\mathbf{k}, \mathbf{q}, -\mathbf{q}) P_L(q) \\ & + P_{\text{ctr}}(\mathbf{k}) + P_{\text{stoch}}(k), \end{aligned} \quad (6)$$

with  $Z_1(\mathbf{k}), Z_2(\mathbf{k}_1, \mathbf{k}_2)$  and  $Z_3(\mathbf{k}_1, \mathbf{k}_2, \mathbf{k}_3)$  the redshift space kernels for the SPT loop corrections (Scoccimarro et al. 1999b), and  $P_L$  being the IR-resummed linear power spectrum (Baldauf et al. 2015a; Blas et al. 2016). The stochastic power spectrum is given by (Eggemeier et al. 2020)

$$P_{\text{stoch}}(k) = (1 + \alpha_P + \epsilon_{k^2} k^2) \bar{n}^{-1}, \quad (7)$$

with two free parameters,  $\alpha_P$  and  $\epsilon_{k^2}$ , describing a constant deviation from purely Poisson shot noise  $\bar{n}^{-1}$ , and higher-order scale dependent corrections generated to account for the short-range non-locality, respectively. The physical meaning of  $\alpha_P$  can be explained with the halo exclusion effect (Smith et al. 2007; Baldauf et al. 2013b); its value can be either positive (e.g., in galaxy populations with high satellite fractions) or negative (e.g., in central galaxies of massive halos) (Baldauf et al. 2013b). The term  $(1 + \alpha_P) \bar{n}^{-1}$  corresponds to the noise parameter  $N$  usually used in the literature, which denotes a scale-independent noise power spectrum. In this work we include scale-dependency into the shot noise, a feature which is supported by numerical simulations (Ginzburg et al. 2017). Furthermore, as we show below, the data prefers a strong scale-dependence in the shot noise (see subsection 4.1 and Figure 2).

The redshift space loop corrections lead to 28 independent integrals, which we compute using the Fast-PT algorithm (McEwen et al. 2016; Fang et al. 2017). The EFTofLSS counterterms for this model are

$$\begin{aligned} P_{\text{ctr}}(k, \mu) = & -2 \tilde{c}_0 k^2 P_L(k) - 2 \tilde{c}_2 k^2 f \mu^2 P_L(k) \\ & - 2 \tilde{c}_4 k^2 f^2 \mu^4 P_L(k) + P_{\text{ctr}, \nabla^4 \delta}(k, \mu), \end{aligned} \quad (8)$$

with an additional counterterm proportional to  $\mu^4 k^4 P_L(k)$  to include higher-order contributions and model to some extent the Finger of God effect (FoG):

$$P_{\text{ctr}, \nabla^4 \delta}(k, \mu) = c_{\nabla^4 \delta} k^4 f^4 \mu^4 (b_1 + f \mu^2)^2 P_L(k). \quad (9)$$

This power spectrum model includes in total 10 parameters:  $\{b_1, b_2, b_{\mathcal{G}_2}, b_{\Gamma_3}, \tilde{c}_0, \tilde{c}_2, \tilde{c}_4, \alpha_P, \epsilon_{k^2}, c_{\nabla^4 \delta}\}$ .

For the tree-level bispectrum the expression at tree-level is given by

$$\begin{aligned} B_g(\mathbf{k}_1, \mathbf{k}_2, \hat{s}) = & B_{\text{stoch}}(\mathbf{k}_1, \mathbf{k}_2, \hat{s}) \\ & + \sum_{\mathbf{k}_1 \leq \mathbf{k}_i \leq \mathbf{k}_j \leq \mathbf{k}_3} 2 Z_1(\mathbf{k}_i) Z_1(\mathbf{k}_j) Z_2(\mathbf{k}_i, \mathbf{k}_j) P_L(k_i) P_L(k_j), \end{aligned} \quad (10)$$

with the stochastic contribution

$$B_{\text{stoch}}(\mathbf{k}_1, \mathbf{k}_2, \hat{s}) = (1 + \alpha_B) \bar{n}^{-1} \sum_{i=1}^3 Z_1^2(\mathbf{k}_i) P_L(k_i), \quad (11)$$

where  $\alpha_B$  describes a deviation from the Poisson limit. In contrast to Ivanov et al. (2022), we do not include the FoG modelling and its corresponding parameter in our tree-level model, since such a

contribution is expected only at 1-loop level. This leaves the halo bispectrum to be described by 4 parameters:  $\{b_1, b_2, b_{\mathcal{G}_2}, \alpha_B\}$ .

Overall, we express our theoretical prediction in terms of multipoles, in order to eliminate the  $\mu$ -dependence. For the power spectrum we compute

$$P_l(k) = \frac{2l+1}{2} \int_{-1}^1 d\mu P_{hh}(k, \mu) \mathcal{P}_l(\mu) \quad (12)$$

where  $\mathcal{P}_l(\mu)$  are the Legendre polynomials of order  $l$  and  $P_{hh}(k, \mu)$  is the redshift space power spectrum given by [Equation 6](#). In this analysis we use the monopole ( $l = 0$ ), quadrupole ( $l = 2$ ), and hexadecapole ( $l = 4$ ). Studies have shown that these three multipoles contain most of the cosmological information (e.g., [Taruya et al. 2010](#); [Beutler et al. 2014](#); [Markovic et al. 2019](#)).

An analogous expansion can be applied to the bispectrum, by expanding in terms of spherical harmonics as

$$B_h(k_1, k_2, k_3, \theta, \xi) = \sum_l \sum_{m=-l}^l B_{lm}(k_1, k_2, k_3) Y_l^m(\theta, \xi) \quad (13)$$

with the same convention for triangle description as above ([Scoccimarro et al. 1999a](#)). The expansion coefficients are given by

$$B_{lm}(k_1, k_2, k_3) = \int_{-1}^1 d\cos\theta \int_0^{2\pi} d\xi B_h(k_1, k_2, k_3, \theta, \xi) Y_l^m(\theta, \xi). \quad (14)$$

As is typical in the literature, when we describe the redshift space multipoles of the bispectrum, we consider only the case with  $m = 0$ , as it has been shown that such seemingly strong compression does not lead to a significant loss of information ([Gagran & Samushia 2017](#)). This allows us to write the bispectrum version of [Equation 12](#), since the spherical harmonics reduce to Legendre polynomials in the  $m = 0$  case:

$$B_l(k_1, k_2, k_3) = \frac{2l+1}{2} \times \int_{-1}^1 d\cos\theta \left[ \frac{1}{2\pi} \int_0^{2\pi} d\xi B_h(k_1, k_2, k_3, \theta, \xi) \right] \mathcal{P}_l(\cos\theta). \quad (15)$$

Let us briefly list the known degeneracies, which follow from previous studies, our tests and theory directly:

(i)  $f - b_1$  are anti-correlated: both parameters control the amplitude on large scales, they occur combined with various powers in the model, hence if one gets larger the other should decrease.

(ii) The counterterms  $\tilde{c}_0, \tilde{c}_2, \tilde{c}_4$  and  $c_{\nabla^4\delta}$  are all slightly degenerate with one another, but especially strong is the anti-correlation between  $\tilde{c}_4$  and  $\tilde{c}_2$ . This becomes clear after the projection of [Equation 8](#) into multipoles: for the monopole the first three terms in this equation yield  $-1/2(2\tilde{c}_0 + 0.7\tilde{c}_2f + 0.4\tilde{c}_4f^2)k^2P_L$ , while for the quadrupole we obtain  $-5/2(0.3\tilde{c}_2f + 0.2\tilde{c}_4f^2)k^2fP_L$ . For instance, for  $f \approx 1$  the counterterm parameters  $\tilde{c}_4$  and  $\tilde{c}_2$  cancel each other out if  $\tilde{c}_4 \approx -\tilde{c}_2$ . In these ad-hoc calculations, we have neglected the angle-dependence in the linear power spectrum due to IR-resummation, which however will affect the counterterms in the same way and does not impact our argument. Additionally,  $\tilde{c}_4$  cannot be constrained without the power spectrum hexadecapole data. This can be seen directly from [Equation 8](#) where there are three terms with coefficients  $\tilde{c}_0, \tilde{c}_2, \tilde{c}_4$  that all of them have a form of  $k^2P_L(k)$ . From this it follows that we need all three multipoles to constrain all three parameters.

(iii) The nonlinear bias parameters  $b_2, b_{\mathcal{G}_2}$  and  $b_{\Gamma_3}$  are all degenerate:  $b_2$  is correlated with  $b_{\mathcal{G}_2}$ , while  $b_{\mathcal{G}_2}$  and  $b_{\Gamma_3}$  are strongly

anti-correlated. The power spectrum model includes overall 30 independent contributions (28 for the loop-corrections and 2 for the shot noise), in which the bias parameters come as products with various powers and various combinations: for instance,  $b_2$  appears as  $b_1b_2, b_2^2, b_2f$ , so that it can be constrained with power spectrum data only, while  $b_{\Gamma_3}$  appears only twice and only linearly in combination with  $b_1$  and  $f$ , which makes it harder to constrain. However, the inclusion of the tree-level bispectrum solves this issue, since the bispectrum model does not include  $b_{\Gamma_3}$ . Additionally, due to the absence of  $b_{\Gamma_3}$ ,  $b_2$  and  $b_{\mathcal{G}_2}$  are better constrained since the strong degeneracy is not present anymore. Therefore, we expect measurements of  $b_2$  and  $b_{\mathcal{G}_2}$  to be more precise from bispectrum measurements only, although  $b_1$  is better constrained by power spectrum only measurements.

(iv) The noise parameters are anti-correlated with one another since they both control the deviation from Poisson shot noise (constant and scale-dependent). They dominate on small scales together with other effects like FoG and the monopole counterterm, hence we expect correlations between  $\alpha_P, \epsilon_{k^2}$  and  $\tilde{c}_0, c_{\nabla^4\delta}$ .

## 4 MCMC ANALYSIS

### 4.1 Data

In this work we analyse halo power spectrum and bispectrum measurements in redshift space from the large set of 298 N-body simulations ([Grieb et al. 2016](#); [Lippich et al. 2019](#)). These follow the evolution of  $1000^3$  dark matter particles in a cubic box of side  $L = 1500 \text{ Mpc } h^{-1}$ , corresponding to a total effective volume of  $\sim 1,000 \text{ Gpc}^3 h^{-3}$ . The mass cut in the halo catalogues is set to  $1.12 \cdot 10^{13} M_{\odot} h^{-1}$ , with a resulting halo mean number density of  $\bar{n} = 2.13 \cdot 10^{-4} h^3 \text{ Mpc}^{-3}$ . We limit this study to a single redshift  $z = 1$ . The binning scheme we apply is given by:  $k_i = (2 + (i-1))k_f$ , with the fundamental frequency  $k_f = 2\pi L^{-1}$ , the bin size is  $\Delta k = k_f$ , and the total number of bins is  $N_k = 128$  for the power spectrum and  $N_k = 29$  for the bispectrum (with a total number of triangles  $N_t = 2766$ ). For a detailed description of the measurements, the halo catalog construction and the estimators, we refer the reader to [Oddo et al. \(2021, 2020\)](#); [Rizzo et al. \(2022\)](#).

The fiducial cosmology of the simulations is the  $\Lambda$ CDM best-fit of the combined analysis of WMAP and BOSS DR9 results ([Sánchez et al. 2013](#)) and is given by:  $h = 0.695, \Omega_m = 0.285, \Omega_b = 0.046, n_s = 0.9632, \sigma_8 = 0.828$ . This means that the fiducial IDE parameters we should recover are  $w = -1$  and  $A = 0$ .

### 4.2 Covariance

The covariance matrix is constructed from 10,000 mock halo catalogues produced with the Pinocchio code ([Monaco et al. 2002](#); [Munari et al. 2017](#)), 298 of which have initial conditions chosen to match the initial conditions of the 298 Minerva simulations, while the rest have different initial seeds. The total halo power spectrum of the mock catalogs is matched to the one of the N-body simulations at large scales by adjusting the mass threshold ([Oddo et al. 2020](#)). The large number of mocks allows us to suppress the noise in the off-diagonal components, giving a more accurate covariance, which allows us to better assess the goodness of the fit of the theoretical models we study.

The uncertainties associated to a measurement inferred from this covariance correspond to the volume of a single realization. However, in our analysis we fit the 298 realizations simultaneously by summing up their log-likelihoods (see [subsection 4.3](#)), thus we effectively fit

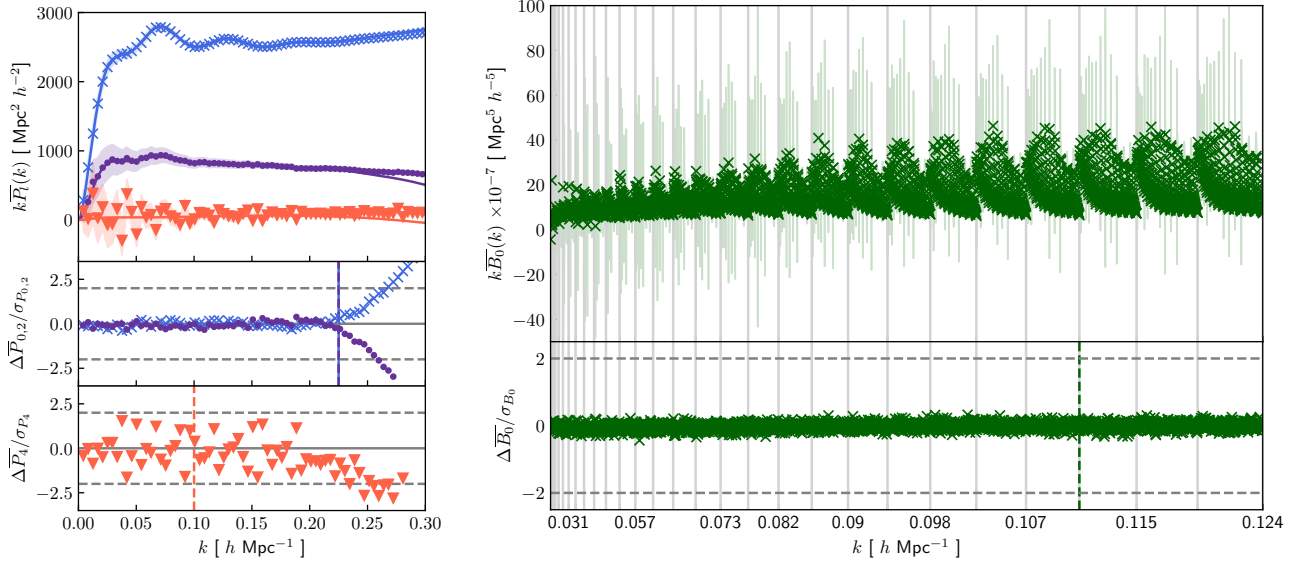


**Figure 2.** Left: average measurements over the 298 Minerva simulations of the halo power spectrum multipoles – monopole (blue crosses), quadrupole (purple dots) and hexadecapole (orange triangles), the solid lines correspond to the posterior-averaged joint model with  $k_{\max,P}^{l=0,2} = 0.225 h \text{ Mpc}^{-1}$ ,  $k_{\max,P}^{l=4} = 0.1 h \text{ Mpc}^{-1}$  and  $k_{\max,B}^{l=0} = 0.111 h \text{ Mpc}^{-1}$ . The large scattering in the residuals of the hexadecapole is a consequence of the effective binning scheme we adopt in the theoretical prediction. Right: the halo bispectrum monopole average (green crosses). The average is taken over the 298 N-body simulations and the Poisson shot noise contribution is not subtracted. Shaded areas denote the uncertainties on the mean. The bottom panels show the relative error on the residuals of the chain-averaged joint model and the mean of the data. The dashed vertical lines correspond to the value of  $k_{\max}$  used in the fit.

for the full simulation volume of  $\sim 1000 \text{ Gpc}^3 h^{-3}$ . This volume is unrealistically large when compared to a typical redshift survey, but can be used to study the theoretical systematics of the model. To perform a more realistic analysis, the volume can be decreased in two ways:

(i) Fitting fewer measurements: it is sufficient to decrease the number of measurements (e.g., in our case 4 realizations correspond to  $13.5 \text{ Gpc}^3 h^{-3}$ ), while using the same covariance for a single measurement. However, during various tests we found that the resulting parameters and the goodness-of-fit vary substantially depending on the particular set of simulations selected. We interpret this as a consequence of the fact that the volume of a single simulation is large, since we obtain large amount of low wave-number modes, which are heavily affected by cosmic variance.

(ii) Rescaling the covariance: this mimics the effect of analysing a subset of measurements, but with the same suppression in cosmic variance as if we were fitting all of them. Unfortunately, due to the artificial rescaling of the covariance we cannot use the traditional measure of goodness-of-fit, the  $\chi^2$ -statistic, because the increased error bars do not match the scatter in the measurements.

In order to mimic the error budget of Stage-IV spectroscopic galaxy surveys, we rescale the measured covariance  $C_{ij}$  by a factor  $\eta$ :

$$C_{ij}^{\text{resc}} = \frac{\eta}{N_R + N_C} \sum_{\alpha=1}^{N_R + N_C} (X_i^\alpha - \bar{X}_i)(Y_j^\alpha - \bar{Y}_j), \quad (16)$$

where  $N_R$  and  $N_C$  are the number of measurements from the simulations and catalogs,  $X, Y \in \{P_{l_1}, B_{l_2}\}$  with  $l$  being the multipole order,  $\alpha$  is the realization index,  $i$  and  $j$  denote indices of the wave-number or triangle configuration bin. This factor  $\eta$  is a ratio between the effective volumes of all simulation realisations and a typical Stage-IV survey with  $V \sim 8 \text{ Gpc}^3 h^{-3}$  at  $z = 1$ , giving  $\eta \approx 126$ . The effective

volume is computed as (Tegmark 1997)

$$V_{\text{eff}} = \left[ \frac{\bar{n}P_{hh}(k^*)}{1 + \bar{n}P_{hh}(k^*)} \right]^2 V, \quad (17)$$

where  $\bar{n}$  is the mean number density,  $V$  is the volume of the measured simulation and  $k^* = 0.1 h \text{ Mpc}^{-1}$  is the reference scale. This allows us to roughly match our simulation data to that expected from future surveys, giving similar constraining power and signal-to-noise ratio. It also allows us to extend the range of validity of the theoretical model up to higher values of  $k_{\max}$  with respect to the cuts we would have to adopt in the case of the non-rescaled covariance and the full volume of the simulations.

It is important to notice that shot noise is not subtracted from our measurements (both the Minerva and the Pinocchio ones). This is particularly prominent in the power spectrum monopole, as can be seen at small scales in Figure 2. In this figure we show the average of the measurements with the corresponding error bars from the rescaled covariance, the chain averaged model from the joint Bayesian analysis (described below) and their residuals. Notice that the very small scatter in the residuals of the monopole and quadrupole (middle-left panel) is an artifact of our inflated errorbars, while for the hexadecapole (bottom-left panel) we have some residual scatter due to the fact that we evaluate the model on the effective modes rather than performing the full average binning.

#### 4.3 Likelihood evaluation

In a Bayesian framework (Bayes 1763; MacKay 2003), the probability of a model given some data is proportional to the product between the probability of obtaining the data under the assumption that the model is correct and the probability of the model parameters to have the corresponding values. In other words, the posterior dis-

tribution is proportional to the likelihood function multiplied by the prior distribution.

In our analysis we choose the priors on nuisance parameters to be non-informative: they are uniform and very broad. We consider as fiducial values for these parameters the best fit values obtained in previous studies (Oddy et al. 2021; Rizzo et al. 2022). Tests were performed to verify that the prior choice does not influence the parameter inference process. However, the priors on the IDE parameters  $w$  and  $A$  are informative and depend on each other. The equation of state parameter  $w$  has a flat prior with size  $[-2, -0.5]$ . For  $w < -2$  dark energy starts to dominate over matter at a later epoch than our redshift of interest  $z = 1$ , so that the growth rate converges quickly to 1 independent from  $\xi$  as in the matter-dominated epoch. As for the upper bound, we have observational evidence of the late time acceleration, which implies  $w < -1/3$ . The parameter  $A$  also has a flat prior with size  $[-20, 20]$ , but with the additional condition that  $A$  must have the same sign as  $1 + w$ . The upper limit for  $A$  is given under the consideration of the upper bound for  $w$  and the most extreme value of  $\xi = 50$  b GeV $^{-1}$  tested out in simulations (Baldi & Simpson 2015), while the lower limit is chosen to have a symmetric prior around the fiducial value of  $A = 0$ . The additional condition on the sign is explained by the fact that the parameter  $\xi = A/(1 + w)$  has to be non-negative, since it represents the ratio of two positive quantities: the cross section of dark sector interactions and the mass of dark energy particles (see discussion at the end of section 2).

Given  $N_R = 298$  independent realizations, we evaluate the total likelihood as the product of individual likelihoods, under the assumption that each is well described by a multivariate Gaussian. As already mentioned, instead of fitting the mean of all realizations with the total volume covariance, we fit each individual simulation and compute

$$-2 \ln \mathcal{L}_{\text{tot}} = -2 \sum_{\alpha}^{N_R} \ln \mathcal{L}_{\alpha} = -\sum_{\alpha}^{N_R} \chi_{\alpha}^2 = \sum_{\alpha=1}^{N_R} \sum_{i,j=1}^{N_b} \left( X_i^{\alpha} - X_i^{\text{theo}} \right) C_{X,i,j}^{-1} \left( X_j^{\alpha} - X_j^{\text{theo}} \right), \quad (18)$$

where  $X_i^{\alpha}$  is the power spectrum or bispectrum multipole measurement from the  $\alpha$ -realization of the  $i$ -th Fourier bin from the total number of bins  $N_b$ ,  $X_i^{\text{theo}}$  is the theoretical prediction and  $C_{ij}$  is the rescaled covariance matrix from equation Equation 16. We also test applying the correction to the likelihood function suggested in Selentini & Heavens (2016), which should take into account the finite number of mocks used in the construction of the covariance matrix:

$$-2 \ln \mathcal{L}_{\alpha} = N_M \ln \left( 1 + \frac{\chi_{\alpha}^2}{N_M - 1} \right), \quad (19)$$

where  $N_M$  is the number of mock catalogs. We found no impact on the posterior distributions, which confirms our expectation of a negligible effect given the large number of mocks catalogues used.

Our likelihood pipeline uses the `emcee` package (Foreman-Mackey et al. 2013) to sample the posterior distribution. We run the MCMC with 300 walkers, and assume them to have reached convergence after 30000 steps in the analysis which only includes the power spectrum multipoles, and after 15000 steps when the bispectrum multipole(s) is (are) included.

#### 4.4 Model evaluation

The evaluation of the theoretical model should in principle be performed on the same grid that is used for the measurements, and the

model should be binned in the same way. This can be understood as the resolution of the following discrepancy: the theoretical prediction assumes an infinite universe with an infinite number of  $k$ -values, while in our case the measurements are performed in boxes with periodic boundary conditions, hence over a restricted number of  $k$ -bins. In general, there are four approaches to resolve this:

(i) Full binning: compute an exact average of the theoretical predictions for the observables over each bin in Fourier space. In other words, calculate the theoretical model at each  $q_i \in k_i$ , with  $k_i$  being a Fourier bin and  $q_i$  denoting all discrete wave-numbers in a bin of size  $\Delta k_i$ , and then find a mean value. In our work the bin size equals the fundamental frequency  $\Delta k = 2\pi/L$ . Advantage: this is the most consistent way; disadvantage: it is computationally demanding especially when re-computing the model at each step of the likelihood evaluation.

(ii) Effective binning: evaluate the theoretical predictions only at one “effective” wave-number, which is computed as the average over each bin centered at  $k$  for the power spectrum multipoles, while for the bispectrum the “effective” triplet is computed in a similar but hierarchical way (see equation B.2 in Rizzo et al. 2022). Advantage: less computationally expensive; disadvantage: it might introduce systematic errors comparable to the statistical uncertainties for the full volume of our data set (Oddy et al. 2020).

(iii) Expansion approach (Oddy et al. 2021): this is an extension of the effective approach which includes a Taylor expansion of the theoretical model around the effective wave-number up to second order. Advantage: high accuracy, especially for the hexadecapole of the power spectrum; disadvantage: it can be computationally demanding if a large number of terms is involved.

(iv) Integration approach: similar to the averaging approach, but the integral is computed instead of building an average as a sum over the multipoles, divided by the number of all discrete vectors in a bin. This approach is popular in the literature (e.g., Ivanov et al. 2022; Eggemeier et al. 2021) but similarly to the effective binning it can introduce non-negligible systematic errors, especially for folded triangles. However, this issue can be bypassed by introducing “discreteness weights” as corrections (Ivanov et al. 2022).

In our study we choose the effective binning for power spectrum and bispectrum multipoles. Our tests show that this type of binning does not have an impact on the inferred parameters due to the enhanced size of our uncertainties after rescaling the covariance, while being the most computationally efficient.

We also note that in the bispectrum case we include all triangular configurations with  $k_1 \geq k_2 \geq k_3$  in our analysis, and do not separate them into squeezed/equilateral/isosceles configurations as is common in the literature. Previous studies (e.g., Oddy et al. 2020; Eggemeier et al. 2021; Smith et al. 2008) show that the signal-to-noise ratio and the accuracy of a model increase for high  $k_{\text{max}}$  if nearly equilateral triangle bins are excluded, while still including elongated triangle configurations. Whether or not this selection improves our constraints of dark energy models when adopting realistic error bars is a subject of our future studies. However, we expect the effect to be minimal.

#### 4.5 Model selection

Our goal is to determine the appropriate scale cuts and forecast the constraining power of future surveys for the IDE parameters,  $w$  and  $A$ . It is crucial to determine the largest range of scales which can be used to extract information from the data in an unbiased manner and tighten the cosmological constraints. This can be also achieved

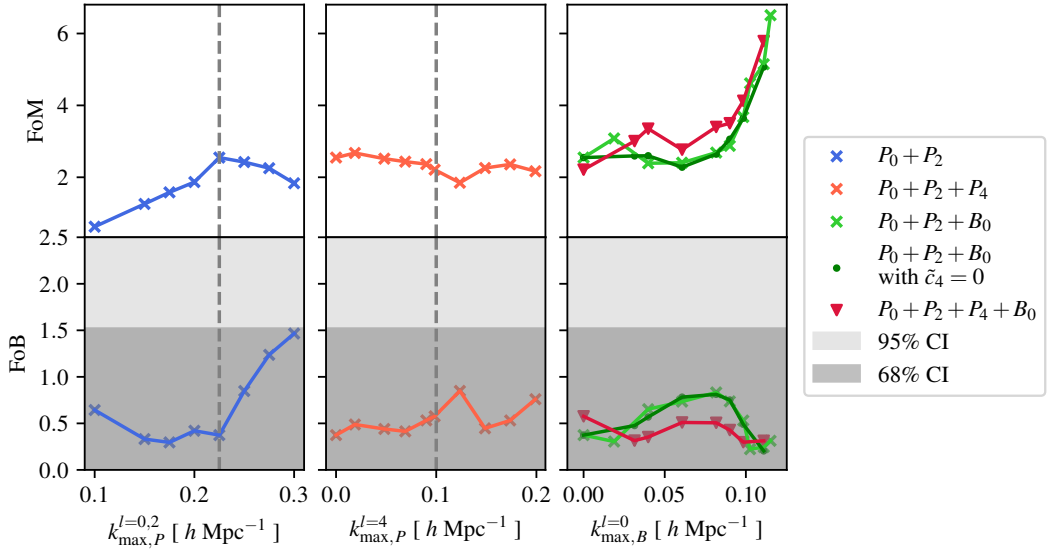


**Figure 3.** Left: performance metrics as a function of the maximum wave-number of the monopole and quadrupole (blue crosses). Middle: performance metrics with the inclusion of the hexadecapole (orange crosses) and with the best scale cut  $k_{\max, P}^{l=0,2} = 0.225 h \text{ Mpc}^{-1}$  from the left panel. Right: joint models — the power spectrum monopole and quadrupole with the bispectrum monopole (light-green crosses), the power spectrum monopole and quadrupole with the bispectrum monopole and one counterterm parameter set to zero (dark-green dots), all power spectrum multipoles with  $k_{\max, P}^{l=4} = 0.1 h \text{ Mpc}^{-1}$  and the bispectrum monopole (dark-red triangles). The dashed grey lines correspond to the values of  $k_{\max}$ . The confidence intervals for FoB are calculated by direct integration of a two-dimensional Gaussian over an ellipse between  $\pm \text{FoB}$  and equating the integral to the 68% and 95% percentile thresholds, which results in FoB equal to 1.52 and 2.49, respectively.

by removing or alleviating degeneracies between the parameters of the theoretical model. For instance, bias relations (i.e., the relations between bias parameters based on their connection due to the underlying physics of gravitational collapse) are able to reduce the parameter space without introducing bias in the estimated parameters. In order to evaluate whether a certain scale cut or a reduction of degeneracies in parameter space provide a better description of the observables we need a way to quantitatively compare the posterior distributions from our Markov chains. Since the  $\chi^2$ -statistic is not valid anymore as a measurement of the goodness-of-fit, due to the rescaling of the covariance matrix (see discussion in subsection 4.2), we make use of two performance metrics to select the best scale cut and/or reduced model (see a similar approach in Eggemeier et al. 2020; Osato et al. 2019):

(i) the Figure of Bias (FoB) quantifies the relative separation of the measured parameters from their fiducial values in terms of the variance of the posterior distribution. We calculate the 68% - 95% percentile thresholds for the FoB by assuming the posterior distribution of the parameters of interest to be Gaussian. Hence, for one parameter the 68% threshold equals 1, while for two parameters the integration of two-dimensional Gaussian over an ellipse results in a FoB of 1.52. It is defined as

$$\text{FoB} = \sqrt{(\theta_{\text{fid}} - \bar{\theta}) S^{-1} (\theta_{\text{fid}} - \bar{\theta})}, \quad (20)$$

where  $\bar{\theta}$  and  $\theta_{\text{fid}}$  are vectors labeling, respectively, the posterior averages and fiducial values of the parameters we want to measure, and  $S = \text{cov}(\theta)$  is the covariance matrix of the parameters calculated from the chains. In our case,  $\theta = [w, A]$  and  $\theta_{\text{fid}} = [-1, 0]$ ;

(ii) the Figure of Merit (FoM) shows the merit of the considered model with respect to the parameters varied in the fit. It is the inverse of the volume of the 68% contours of the parameters, effectively giving a global measure of the inverse size of the uncertainties obtained

on the parameters (Wang 2008). This is given by

$$\text{FoM} = \frac{1}{\sqrt{\det(S)}}. \quad (21)$$

## 5 RESULTS

### 5.1 Joint base model

In total our base model contains 13 parameters:  $\{w, A, b_1, b_2, b_{\mathcal{G}_2}, b_{\Gamma_3}, \tilde{c}_0, \tilde{c}_2, \tilde{c}_4, \alpha_P, \epsilon_{k^2}, c_{\nabla^4 \delta}, \alpha_B\}$ . Firstly, we aim to find the highest  $k_{\max}$  at which the model parameters are not biased while the constraints on the dark energy parameters are the most informative (i.e., FoM reaches its maximum). For this purpose we run our likelihood pipeline, calculate the performance metrics and check the posterior distributions for the nuisance parameters. The latter is done in order to avoid any deviation larger than two standard deviations from the fiducial values for  $b_1, b_2, b_{\mathcal{G}_2}, b_{\Gamma_3}, \alpha_P, \epsilon_{k^2}$  and  $\alpha_B$  as determined in the previous analyses of Oddo et al. (2020, 2021); Rizzo et al. (2022). Note that the counterterms in real space and in redshift space are not the same.

We vary the value of  $k_{\max}$  jointly for the power spectrum monopole and quadrupole, as is typically done in analyses of observational data (Beutler et al. 2014). The scale cut is varied in the range of  $k_{\max, P}^{l=0,2} \in [0.1, 0.3] h \text{ Mpc}^{-1}$  and is found to maximize the FoM while keeping the FoB within one standard deviation at  $0.225 h \text{ Mpc}^{-1}$ . This can be seen in the left panel of Figure 3, where blue crosses correspond to the joint analysis of the lower order power spectrum multipoles. Keeping this value fixed, we then add the hexadecapole with  $k_{\max, P}^{l=4} \in [0, 0.2] h \text{ Mpc}^{-1}$ . We expect our model to describe it less efficiently than the lower order multipoles, therefore the range of scales included for  $P_4$  is smaller than for  $P_0$  and  $P_2$ . Unsurprisingly the addition of the hexadecapole allows us to constrain

$\tilde{c}_4$  and hence improve significantly the constraints on  $\tilde{c}_2$ , as well as on the other counterterms, though less significantly. However, we see in the middle panel of Figure 3 no improvement in the constraints of the IDE parameters, the hexadecapole only slightly decreases the FoM and increases the FoB. This finding is in agreement with the conclusions of Carrilho et al. (2021).

Next we include the bispectrum monopole,  $B_0$ . This is shown in the right panel of Figure 3. We perform the analysis by adding it to  $P_0 + P_2$ , since the power spectrum hexadecapole does not contribute to the improvement of the constraints in the IDE parameters. The results are denoted by the light green crosses connected by a solid line. We observe an increase in the FoB and no improvement in the FoM for scales up to  $k_{\max, B}^{l=0} = 0.08 h \text{ Mpc}^{-1}$  for  $P_0 + P_2 + B_0$ . However, for  $k_{\max, B}^{l=0} > 0.08 h \text{ Mpc}^{-1}$  we notice a steep growth in the FoM as we add more  $k$ -bins. Clearly, inclusion of the small-scale information contained in the higher  $k$ -bins provides better constraining power, especially since the number of triangles increases significantly with each bin. The results do not show a bias in any of the parameters of the model, at least up to the 27-th  $k$ -bin (corresponding to  $k_{\max, B}^{l=0} = 1.12 h \text{ Mpc}^{-1}$ ) from the total 29 bins of our measurements.

Additionally, we perform a joint analysis with the hexadecapole of the power spectrum included up to  $0.1 h \text{ Mpc}^{-1}$ , which is rather conservative and common in the literature. This model with all power spectrum multipoles and  $B_0$  shows a mild but continuous improvement of the FoM in comparison to the model with only lower order power spectrum multipoles (see the dark red triangles in the right panel). Noticeably, adding the power spectrum hexadecapole in the joint analysis with the bispectrum monopole always results in a smaller FoB (and thus bias) of the IDE parameters. We check whether the same effect could be achieved by setting the otherwise unconstrained  $\tilde{c}_4$  to zero in the model with the monopole and quadrupole only. As expected, the constraints of the  $P_0 + P_2 + B_0$  model are not sensitive to this change. This is shown by the dark-green dots in the right panel, which overlap with the light-green crosses of the base model with  $\tilde{c}_4 \neq 0$ . We therefore conclude that the inclusion of the hexadecapole of the power spectrum, in combination with the bispectrum monopole, can help (especially at lower scale cuts) by breaking degeneracies between the counterterms and bias parameters.

The full posterior plot is shown in Figure A1 of section A. Additionally, we present in Figure 4 the triangle plot for the marginalized posterior distribution of the IDE parameters. The characteristic ‘‘butterfly’’ pattern, in which the posterior distribution is present only in two quadrants – upper-right and lower-left, is the consequence of the priors on the IDE parameters with the condition  $A/(1+w) \geq 0$ , as described in subsection 4.3. The  $w - A$  contour shows a strong degeneracy: as argued in section 2, a very negative value of  $w$  leads to a later start of the dark energy dominated epoch, hence to a longer matter domination which is associated with increased growth of structures. A negative value of  $A$  leads to extra drag in Equation 2, and thus to an enhancement of the growth of structures in the linear regime (the opposite is true for the nonlinear regime, as discussed in section 2). On large scales the drag term acts in the same direction as the gravitational acceleration, since the velocity field is always aligned with the spatial gradient of the gravitational potential in the linear regime. The opposite happens for  $w > -1$  and  $A > 0$ . This is in line with what can already be seen in Figure 1 and its diagonal (from upper left to lower right) pattern in the growth rate  $f$ , and is particularly prominent in the upper right corner (for positive values of  $A$  and  $(1+w)$ ). There we observe the same level of suppression for either a larger  $w$  value with  $A$  fixed, or for a larger  $A$  value with  $w$  fixed. It is therefore apparent how the two effects are strongly de-

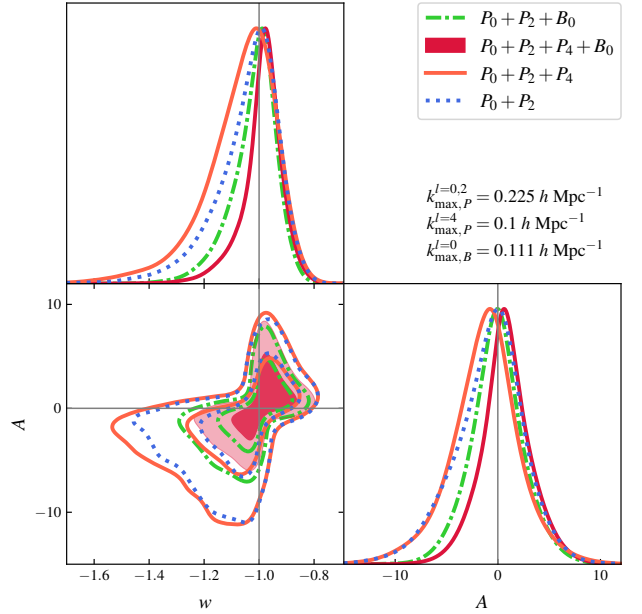


**Figure 4.** Marginal posterior distributions for the IDE parameters with the base model and scale cuts as specified in the plot. The power spectrum monopole and quadrupole analysis is denoted by the dotted blue line, constraints from all power spectrum multipoles are given by the solid orange line, the joint analysis of the power spectrum monopole plus quadrupole and bispectrum monopole is presented with the dotted-dashed light-green line, and the full joint analysis is shown with the dark-red line. The fact that the contour shows non-vanishing values for the forbidden regions  $A/(1+w) < 0$  is an artifact of the smoothing used for plotting. Thin grey lines correspond to the fiducial values.

generate, which results in larger uncertainties on them, especially in biased cases. Such a conclusion is in agreement with the findings of Carrilho et al. (2021).

In addition to the base model with 13 parameters, we run the joint analysis adopting some assumptions that are common in the literature:  $b_{\Gamma_3} = 0$  and / or  $\epsilon_{k^2} = 0$ . Assuming that noise is scale-independent (as opposed to leaving the  $\epsilon_{k^2}$  parameter free), results in no improvement and no bias in the constraints. This is a consequence of the rescaled error bars, since we know from the real space analysis with the full volume of the simulations by Oddo et al. (2021) that the scale-dependent term in shot noise is relevant at larger Fourier modes due to accounting for additional corrections beyond the assumed one-loop model. The assumption of  $b_{\Gamma_3} = 0$  does not yield improved constraints, but it biases the noise parameters  $\alpha_P$ ,  $\epsilon_{k^2}$  and  $\alpha_B$  by more than  $2\sigma$  with respect to the fiducial values. This is in line with the joint analysis performed on the same data set in real space, which measures  $b_{\Gamma_3} = 0$  to be inconsistent with zero at more than  $2\sigma$  (Oddo et al. 2021). The assumption of both conditions results in bias in the noise parameters and  $b_{\mathcal{G}_2}$  at more than  $2\sigma$  level, while  $\alpha_B$  gets biased at more than  $3\sigma$  level. From this we conclude that, when including the bispectrum monopole,  $b_{\Gamma_3}$  should not be set to zero.

## 5.2 Bias relations

Although the strong degeneracy between  $b_{\mathcal{G}_2}$  and  $b_{\Gamma_3}$  is broken by the inclusion of the bispectrum monopole in the analysis, we are still interested in the impact of bias relations for two reasons: firstly, to

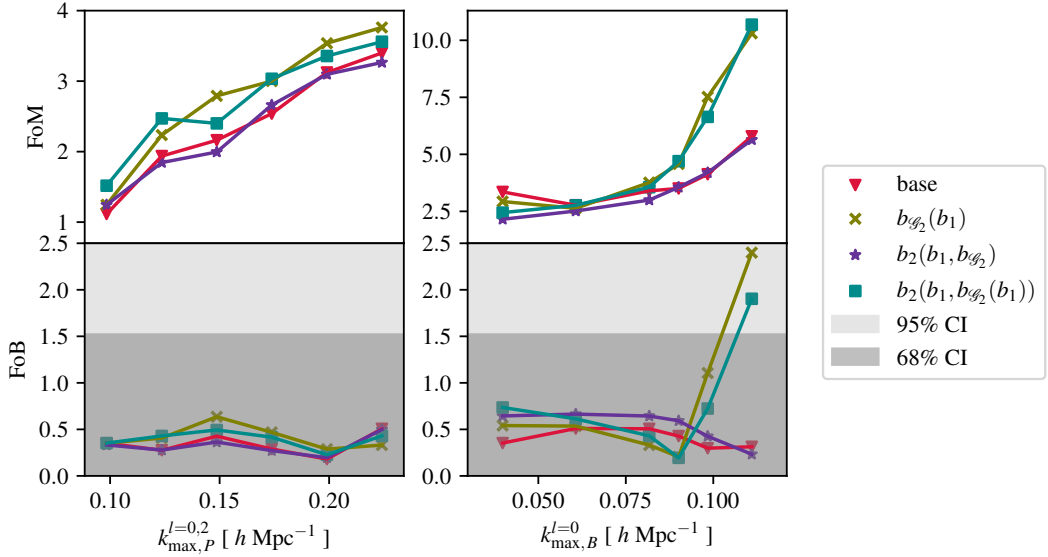


**Figure 5.** Joint analysis of all power spectrum multipoles and the bispectrum monopole. Left: performance metrics as a function of the maximum wave-number of the power spectrum monopole and quadrupole with  $k_{\max,B}^{l=0} = 0.08 h \text{ Mpc}^{-1}$ . Right: performance metrics as a function of the maximum wave-number of the bispectrum monopole with  $k_{\max,P}^{l=0,2} = 0.225 h \text{ Mpc}^{-1}$  and  $k_{\max,P}^{l=4} = 0.1 h \text{ Mpc}^{-1}$ . Dark-red triangles correspond to the base model with 13 parameters, olive crosses denote the tidal bias relation, purple stars represent the  $b_2$ -relation, the dark-cyan squares denote the combined relation of  $b_2$  and  $b_{\mathcal{G}_2}$ . The confidence intervals for FoB are calculated as in Figure 3.

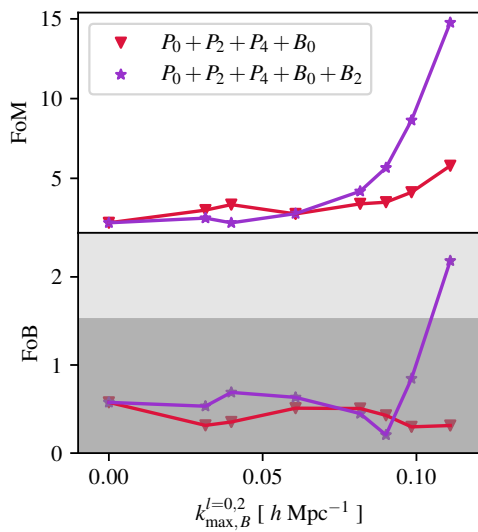


**Figure 6.** Joint analysis of all power spectrum multipoles with the bispectrum monopole (dark-red triangles) and quadrupole (purple stars). The performance metrics, FoM and FoB, are presented as a function of the maximum wave-number on both multipoles of the bispectrum. The confidence intervals for the FoB are calculated as in Figure 3.

reduce the dimensionality of the parameter space; secondly, we know that both  $A$  and  $w$  are correlated with  $b_1$ , hence a tighter constraint on the latter will lead to tighter constraints on the IDE parameters.

We investigate the full joint analysis of  $P_0 + P_2 + P_4 + B_0$  for the following bias relations:

(i) the fit from the separate universe simulations presented in

Lazeyras et al. (2016):

$$b_2(b_1, b_{\mathcal{G}_2}) = 0.412 - 2.143b_1 + 0.929b_1^2 + 0.008b_1^3 + \frac{4}{3}b_{\mathcal{G}_2}; \quad (22)$$

(ii) the fit from the excursion set approach of Eggemeier et al. (2020):

$$b_{\mathcal{G}_2}(b_1) = 0.524 - 0.547b_1 + 0.046b_1^2; \quad (23)$$

(iii) the combination of both relations:  $b_2(b_1, b_{\mathcal{G}_2}(b_1))$ .

These relations have been shown to improve the fits of the power spectrum and bispectrum in Oddo et al. (2020, 2021); Rizzo et al. (2022). Results for the individual relations as well as for the combined one are shown in Figure 5 in terms of the FoM and FoB metrics. We notice that the  $b_2(b_1, b_{\mathcal{G}_2})$  relation, denoted by purple stars, does not impact our constraints both when varying the maximum wave-number for the power spectrum (left panel) and for the bispectrum (right panel). This can be explained by a combination of two factors. Firstly, the fact that in our base model the  $b_2$ -relation always stays consistent with the fiducial value of  $b_2$ , (that measured from the real space analysis of Oddo et al. 2020, 2021; Rizzo et al. 2022), which implies that we are not introducing any new information with the bias relation. Then, while a different behaviour has been seen in the analysis of Oddo et al. (2021) in Fig. 8 with very small error bars, the fact that ours are “realistic” (larger) for Stage-IV surveys means that we cannot detect this effect. On the other hand, the tidal bias relation (olive crosses) and its combination with the  $b_2$ -relation (dark-cyan squares) lead to a reduction in the constraints on  $w$ ,  $A$ ,  $b_1$  and  $b_2$ . This improvement is particularly prominent in the right panel, where the number of modes in the bispectrum monopole is varied while the scale-range of power spectrum multipoles is fixed. At  $k_{\max,B}^{l=0} = 0.1 h \text{ Mpc}^{-1}$  we see the  $b_{\mathcal{G}_2}(b_1)$  has a higher value of FoM, which equals  $\approx 7.5$  and is larger than FoM  $\approx 4$  of the base model with the same largest Fourier mode. However, for  $k_{\max,B}^{l=0} > 0.1 h \text{ Mpc}^{-1}$  cases (ii) and (iii) cause a continuous shift of the IDE parameters to the positive

values of  $A$  and  $(1 + w)$ . Nonetheless, even for  $k_{\max, B}^{l=0} = 0.111 h \text{ Mpc}^{-1}$  all nuisance and IDE parameters stay within 2 standard deviations of their fiducial values (see the full posterior distribution in [Figure A2](#)), FoM reaches  $\simeq 11$  for both relations. From the lower right panel we see that the combined bias relation results in the less biased dark energy parameters, in contrast to the tidal-relation only.

We note that the bias relations applied here are derived in the context of the  $\Lambda\text{CDM}$  cosmology. From the simulations performed in [Baldi & Simpson \(2015\)](#), we know that at the redshift of our interest deviations of the halo mass function from the standard cosmology are negligible. Moreover, the measurements in our analysis do not include modifications in the gravitational interaction. Therefore, the application of the bias relations is justified. Nevertheless, we aim to study the impact of the interactions between dark matter and dark matter on the bias relations in our future work.

### 5.3 Bispectrum quadrupole

Recent progress in measuring the bispectrum multipoles from simulations ([Rizzo et al. 2022](#)) showed that, while the monopole constrains mostly the bias parameters  $b_1$ ,  $b_2$  and  $b_{G_2}$ , the quadrupole can break the  $b_1 - f$  degeneracy and can constrain the growth factor even in the case of a bispectrum only analysis. These constraints on the growth rate from the bispectrum multipoles are weaker than the ones that can be obtained from the power spectrum multipoles. The argument for the inclusion of higher order multipoles of the bispectrum is also discussed in [Gualdi & Verde \(2020\)](#); [Gualdi et al. \(2021\)](#).

However, it raises the question: if including the bispectrum quadrupole improves the constraints on the growth rate, does it also do so for the IDE parameters  $w$  and  $A$ ? In particular, it is interesting to investigate if this holds also in the case of Stage-IV-like error bars, such as the ones we employ here. We run our likelihood pipeline for the base model and find that indeed, for  $k_{\max, B}^{l=0,2} > 0.09 h \text{ Mpc}^{-1}$ , the addition of the quadrupole improves the constraints on the dark energy parameters. Our results are shown in [Figure 6](#), where dark-red triangles denote the power spectrum multipoles plus the bispectrum monopole, while the addition of  $B_2$  is denoted by purple stars. We note that the FoB and FoM as functions of  $k_{\max}$  resemble the trend obtained in the previous section with the bias relations, with the exception that in the present case the slope of the FoM in the upper panel is steeper at large wave-numbers. For instance, for  $k_{\max, B}^{l=0,2} = 0.1 h \text{ Mpc}^{-1}$ , we get  $\text{FoM} \simeq 9$ , while with the tidal bias relation from the previous section and without the bispectrum quadrupole we obtained  $\text{FoM} \simeq 7.5$ . The full posterior distribution for the  $k_{\max, B}^{l=0,2} = 0.111 h \text{ Mpc}^{-1}$  can be seen in [Figure A3](#). The increase in the FoM is the result of an improvement in the constraints on the IDE parameters and the linear bias. Moreover, because of the degeneracy between the linear bias and the other bias parameters, a tighter constraint on the former leads to the latter being more constrained too. This effect is more significant than in the case of the bias relations, and avoids resorting to such relations, which might not be valid in extended cosmological models. This is a hint that the bispectrum quadrupole might play a crucial role in constraining extended cosmological models with spectroscopic galaxy clustering data.

### 5.4 Forecast for $w\text{CDM}$

In addition to IDE, we repeat our analysis for the simplest extension to  $\Lambda\text{CDM}$  model in which  $w = w_0$  is constant, but can assume values

different from  $-1$ . Based on what we have learned with the IDE model we perform the following analyses:

- (i) base model with  $k_{\max, B}^{l=0} = 0.111 h \text{ Mpc}^{-1}$ ;
- (ii) combined bias relations with  $k_{\max, B}^{l=0} = 0.095 h \text{ Mpc}^{-1}$ ;
- (iii) bispectrum monopole and quadrupole with  $k_{\max, B}^{l=0,2} = 0.09 h \text{ Mpc}^{-1}$ .

We obtain the following constraints on the dark energy equation of state parameter for the three runs respectively:  $w = -0.99 \pm 0.10$ ,  $-0.98 \pm 0.10$ ,  $-0.99 \pm 0.09$ . The full posterior is shown in [Figure A4](#). All three cases result in similar level of uncertainty on the inferred parameters, except on the shot noise parameter of the bispectrum for which both the bias relations and the inclusion of  $B_2$  yield tighter constraints. However, the improvement with respect to the analysis with the power spectrum only is apparent, roughly 38%, demonstrating once again that the inclusion of the bispectrum does increase the cosmological information that can be extracted from the data.

## 6 CONCLUSIONS

In this paper we have performed a detailed analysis of the role of the bispectrum multipoles in constraining an interacting dark energy model. This is relevant for Stage-IV spectroscopic surveys, as a validation test and a comprehensive case study for the joint power spectrum and bispectrum analyses of extended cosmological models.

We modelled the power spectrum and bispectrum multipoles with the EFTofLSS at one-loop and tree-level, respectively. We computed the linear growth factor and the logarithmic growth rate by solving the growth equation for the IDE model. As input data (the fiducial data vector in our likelihood pipeline) we used a large set of simulations at a single redshift  $z = 1$ , complemented with a rescaled numerical covariance constructed from 10,000 mock catalogues. Our fits used an effective volume that mimics the error budget of Stage-IV spectroscopic galaxy surveys, and we run our MCMC analyses with a Gaussian likelihood function.

Using this setup, we first added more observables in sequence and studied them in terms of their ability to constrain the IDE parameters  $w$  and  $A$  without introducing a bias in the dark energy and nuisance parameters of the model. For the latter, we adopted as fiducial values the best fit values from previous studies performed in the context of standard  $\Lambda\text{CDM}$  ([Oddo et al. 2020, 2021; Rizzo et al. 2022; Moretti et al. 2022](#)). We found that the tree-level model for the bispectrum monopole is still valid up to  $k \simeq 0.11 h \text{ Mpc}^{-1}$ , close to the largest value available in our measurements. In contrast to adding the hexadecapole to the lower-order multipoles of the power spectrum, the addition of the bispectrum monopole improved the constraints on the IDE parameters by  $\sim 30\%$  for the equation of state parameter  $w$ , and  $\sim 26\%$  for the coupling parameter  $A$ . We also found that the  $P_0 + P_2 + P_4 + B_0$  combination yields better constraints and less bias in the inferred parameters than  $P_0 + P_2 + B_0$ .

In general, the large number of triangular configurations over which the bispectrum model has to be evaluated when including such nonlinear scales results in a rather computationally expensive analysis. Hence, we studied two approaches, which could allow us to get the same level of constraints but at smaller scales. The first approach aims at reducing the parameter space, which in our base case included 13 parameters, by means of bias relations. We tested the validity of two bias relations, and found that the tidal bias relation and its combination with the  $b_2$  relation are the most suitable for this

goal. In the second approach we added the bispectrum quadrupole to our Bayesian analysis. We found that either applying the bias relations or including the bispectrum quadrupole allows us to efficiently constrain the IDE parameter at more moderate values of  $k_{\max}$  than in the base model  $P_0 + P_2 + P_4 + B_0$ . For instance, to achieve the same level of constraints with  $\text{FoM} \sim 6$  one can use either of the following: a) use only the bispectrum monopole in the base model, but include it up to high Fourier mode of  $k_{\max, B}^{l=0} = 0.11 h \text{ Mpc}^{-1}$ , b) apply the tidal bias relation in the scale range with the highest mode  $k_{\max, B}^{l=0} = 0.095 h \text{ Mpc}^{-1}$ , c) add the quadrupole measurements and evaluate the model up to  $k_{\max, B}^{l=0,2} = 0.09 h \text{ Mpc}^{-1}$ .

We then forecasted the constraining power of Stage-IV spectroscopic galaxy surveys on the IDE parameters and the dark energy equation of state parameter in  $w\text{CDM}$ . At  $z = 1$  we found  $\sigma_w = 0.08$  and  $\sigma_A = 2.51 \text{ b GeV}^{-1}$  for the IDE case, while for the  $w\text{CDM}$  case, we found  $\sigma_w = 0.1$ . The first values are in a good agreement with the results of Carrilho et al. (2021), where  $\sigma_w = 0.06$  and  $\sigma_A = 2 \text{ b GeV}^{-1}$  were found when only power spectrum multipoles were used in the MCMC analysis. However, in Carrilho et al. (2021) the simulated data contained more than one order of magnitude less shot noise in comparison to our case, while the volume of the measurements was smaller with  $V \sim 4 \text{ Gpc}^3 h^{-3}$ . Additionally, the covariance in the previous work was computed analytically up to the linear order, while the one used in this work is based on mocks, which is more realistic and contributes to larger uncertainties on the inferred parameters. For the  $w\text{CDM}$  cosmology, our forecasted constraint with the bispectrum and only one redshift bin outperforms the full-shape analysis (FS) with the EFTofLSS from the BOSS survey of D'Amico et al. (2021). We stress that the analysis of BOSS data takes advantage of two redshift bins and three different sky cuts, with the addition of BAO measurements, while the volume of  $6.5 \text{ Gpc}^3 h^{-3}$  and number density of  $2.2 \times 10^{-4} h^3 \text{ Mpc}^{-3}$  are very comparable with our values. On the other hand, we did not include effects such as the impact of the window function and Alcock-Paczinsky in our analysis. In D'Amico et al. (2021), the authors mention that FS analysis with the power spectrum alone is not sufficient to constraint  $w$ , due to strong degeneracies. They measure  $w = -1.101^{+0.14}_{-0.11}$ , which is still a stronger limit than the one obtained from Planck2018 data with lensing (Planck Collaboration et al. 2020):  $w = -1.57^{+0.16}_{-0.33}$ . These values of  $w$  from the power spectrum analysis are in agreement with our forecast, when the bispectrum is not included (see Figure A4).

A number of interesting questions remain to be answered. The first natural step would be to perform this analysis with the data from the BOSS survey. Additionally, it would be interesting to study the time-dependent dark energy equation of state, for example, in the CPL parametrization (Linder 2003; Chevallier & Polarski 2001), which would allow for different effects of the interaction. This study requires data at different redshift bins, in order to constrain  $w_0$  and  $w_a$ . In the case of IDE, the time-dependent equation of state promises to have weaker impact on the nonlinear scales than the constant- $w$  models Baldi & Simpson (2017). Another potential direction of our study is the inclusion of one-loop effects in the bispectrum model, as was recently done for  $\Lambda\text{CDM}$  cosmology in D'Amico et al. (2022) and Philcox et al. (2022). In the latter the authors show that the one-loop corrections for the bispectrum start to be significant already at  $k_{\max, B}^{l=0} > 0.1 h \text{ Mpc}^{-1}$ . This is also expected to extend the reach of the model and therefore its constraining power.

## ACKNOWLEDGEMENTS

We are grateful to Claudio Dalla Vecchia and Ariel Sánchez for running and making available the Minerva simulations, performed on the Hydra and Euclid clusters at the Max Planck Computing and Data Facility in Garching, and to Pierluigi Monaco, for producing the Pinocchio mocks, run on the GALILEO cluster at CINECA thanks to an agreement with the University of Trieste. We thank Andrea Oddo and Emiliano Sefusatti for the effort in building the initial likelihood code, and for useful conversations. We acknowledge use of the Cuillin computing cluster, Royal Observatory, University of Edinburgh. We acknowledge use of open source software: Python (Van Rossum & Drake Jr 1995; Hunter 2007), numpy (Van Der Walt et al. 2011), scipy (Virtanen et al. 2020), astropy (Astropy Collaboration et al. 2018), corner (Foreman-Mackey 2016), GetDist (Lewis 2019). MT's research is supported by a doctoral studentship in the School of Physics and Astronomy, University of Edinburgh. AP is a UK Research and Innovation Future Leaders Fellow [grant MR/S016066/1]. PC and CM's research is supported by a UK Research and Innovation Future Leaders Fellowship [grant MR/S016066/1]. For the purpose of open access, the author has applied a Creative Commons Attribution (CC BY) licence to any Author Accepted Manuscript version arising from this submission.

## DATA AVAILABILITY

The data underlying this article will be shared on reasonable request to the corresponding author.

## REFERENCES

Abbott T. M. C., et al., 2021, Dark Energy Survey Year 3 Results: Cosmological Constraints from Galaxy Clustering and Weak Lensing ([arXiv:2105.13549](https://arxiv.org/abs/2105.13549))

Aghamousa A., et al., 2016, The DESI Experiment Part I: Science, Targeting, and Survey Design ([arXiv:1611.00036](https://arxiv.org/abs/1611.00036))

Amendola L., 2000, *Phys. Rev. D*, **62**, 043511

Amendola L., Tsujikawa S., 2020, *J. Cosmology Astropart. Phys.*, **2020**, 020

Assassi V., Baumann D., Green D., Zaldarriaga M., 2014, *J. Cosmology Astropart. Phys.*, **2014**, 056

Astropy Collaboration et al., 2018, *AJ*, **156**, 123

Baldauf T., Seljak U., Desjacques V., McDonald P., 2012, *Phys. Rev. D*, **86**, 083540

Baldauf T., Seljak U., Smith R. E., Hamaus N., Desjacques V., 2013a, *Phys. Rev. D*, **88**, 083507

Baldauf T., Seljak U., Smith R. E., Hamaus N., Desjacques V., 2013b, *Phys. Rev. D*, **88**, 083507

Baldauf T., Mirbabayi M., Simonović M., Zaldarriaga M., 2015a, *Phys. Rev. D*, **92**, 043514

Baldauf T., Mercolli L., Mirbabayi M., Pajer E., 2015b, *J. Cosmology Astropart. Phys.*, **2015**, 007

Baldi M., Simpson F., 2015, *MNRAS*, **449**, 2239

Baldi M., Simpson F., 2017, *MNRAS*, **465**, 653

Barros B. J., Amendola L., Barreiro T., Nunes N. J., 2019, *J. Cosmology Astropart. Phys.*, **2019**, 007

Baumann D., Nicolis A., Senatore L., Zaldarriaga M., 2012, *J. Cosmology Astropart. Phys.*, **2012**, 051

Bayes T., 1763, *Phil. Trans. of the Royal Soc. of London*, **53**, 370

Beltrán Jiménez J., Bettini D., Figueruelo D., Teppa Pannia F. A., Tsujikawa S., 2021, *Phys. Rev. D*, **104**, 103503

Bernardeau F., Colombi S., Gaztañaga E., Scoccimarro R., 2002, *Phys. Rep.*, **367**, 1

Bertone G., Hooper D., Silk J., 2005, *Physics Reports*, **405**, 279

Beutler F., et al., 2014, *MNRAS*, **443**, 1065

Beutler F., et al., 2017, *MNRAS*, **466**, 2242

Blas D., Lesgourgues J., Tram T., 2011, *JCAP*, **07**, 034

Blas D., Garny M., Ivanov M. M., Sibiryakov S., 2016, *J. Cosmology Astropart. Phys.*, **2016**, 052

Carrasco J. J. M., Hertzberg M. P., Senatore L., 2012, *Journal of High Energy Physics*, **2012**, 82

Carrilho P., Moretti C., Bose B., Marković K., Pourtsidou A., 2021, *J. Cosmology Astropart. Phys.*, **2021**, 004

Chan K. C., Scoccimarro R., Sheth R. K., 2012, *Phys. Rev. D*, **85**, 083509

Chevallier M., Polarski D., 2001, *International Journal of Modern Physics D*, **10**, 213

Clemson T., Koyama K., Zhao G.-B., Maartens R., Valiviita J., 2012, *Phys. Rev. D*, **85**, 043007

Clifton T., Ferreira P. G., Padilla A., Skordis C., 2012, *Phys. Rep.*, **513**, 1

Copeland E. J., Sami M., Tsujikawa S., 2006, *International Journal of Modern Physics D*, **15**, 1753

Crocce M., Scoccimarro R., 2008, *Phys. Rev. D*, **77**, 023533

D'Amico G., Senatore L., Zhang P., 2021, *J. Cosmology Astropart. Phys.*, **2021**, 006

D'Amico G., Donath Y., Lewandowski M., Senatore L., Zhang P., 2022, arXiv e-prints, p. [arXiv:2206.08327](https://arxiv.org/abs/2206.08327)

Desjacques V., Jeong D., Schmidt F., 2018, *Phys. Rep.*, **733**, 1

Di Valentino E., Melchiorri A., Mena O., 2017, *Phys. Rev. D*, **96**, 043503

Di Valentino E., Melchiorri A., Mena O., Vagnozzi S., 2020a, *Physics of the Dark Universe*, **30**, 100666

Di Valentino E., Melchiorri A., Mena O., Vagnozzi S., 2020b, *Phys. Rev. D*, **101**, 063502

Eggemeier A., Scoccimarro R., Crocce M., Pezzotta A., Sánchez A. G., 2020, *Physical Review D*, **102**, 103530

Eggemeier A., Scoccimarro R., Smith R. E., Crocce M., Pezzotta A., Sánchez A. G., 2021, *Phys. Rev. D*, **103**, 123550

Fang X., Blazek J. A., McEwen J. E., Hirata C. M., 2017, *J. Cosmology Astropart. Phys.*, **2017**, 030

Farrar G. R., Peebles P. J. E., 2004, *ApJ*, **604**, 1

Foreman-Mackey D., 2016, *The Journal of Open Source Software*, **1**, 24

Foreman-Mackey D., Hogg D. W., Lang D., Goodman J., 2013, *PASP*, **125**, 306

Fry J. N., Gaztanaga E., 1993, *ApJ*, **413**, 447

Gagrani P., Samushia L., 2017, *MNRAS*, **467**, 928

Ginzburg D., Desjacques V., Chan K. C., 2017, *Phys. Rev. D*, **96**, 083528

Gómez-Valet A., Pettorino V., Amendola L., 2020, *Phys. Rev. D*, **101**, 123513

Grieb J. N., Sánchez A. G., Salazar-Albornoz S., Dalla Vecchia C., 2016, *MNRAS*, **457**, 1577

Gualdi D., Verde L., 2020, *J. Cosmology Astropart. Phys.*, **2020**, 041

Gualdi D., Gil-Marín H., Verde L., 2021, *J. Cosmology Astropart. Phys.*, **2021**, 008

Hunter J. D., 2007, *Computing In Science & Engineering*, **9**, 90

Ivanov M. M., Philcox O. H. E., Nishimichi T., Simonović M., Takada M., Zaldarriaga M., 2022, *Phys. Rev. D*, **105**, 063512

Ivezić v., et al., 2019, *Astrophys. J.*, **873**, 111

Kase R., Tsujikawa S., 2020, *Physics Letters B*, **804**, 135400

Laureijs R., et al., 2011, Euclid Definition Study Report ([arXiv:1110.3193](https://arxiv.org/abs/1110.3193))

Lazeyras T., Wagner C., Baldauf T., Schmidt F., 2016, *J. Cosmology Astropart. Phys.*, **2016**, 018

Lesgourgues J., 2011, arXiv e-prints, p. [arXiv:1104.2932](https://arxiv.org/abs/1104.2932)

Lewis A., 2019, GetDist: a Python package for analysing Monte Carlo samples ([arXiv:1910.13970](https://arxiv.org/abs/1910.13970))

Lewis A., Challinor A., 2011, CAMB: Code for Anisotropies in the Microwave Background, Astrophysics Source Code Library, record ascl:1102.026 (ascl:1102.026)

Linder E. V., 2003, *Phys. Rev. Lett.*, **90**, 091301

Lippich M., et al., 2019, *MNRAS*, **482**, 1786

MacKay D. J. C., 2003, *Information Theory, Inference, and Learning Algorithms*. Copyright Cambridge University Press

Markovic K., Bose B., Pourtsidou A., 2019, *Open J. Astrophys.*, **2**, 13

McDonald P., Roy A., 2009, *J. Cosmology Astropart. Phys.*, **2009**, 020

McEwen J. E., Fang X., Hirata C. M., Blazek J. A., 2016, *J. Cosmology Astropart. Phys.*, **2016**, 015

Monaco P., Theuns T., Taffoni G., 2002, *MNRAS*, **331**, 587

Moretti C., Rizzo F., Pardede K., Oddo A., Sefusatti E., Porciani C., Monaco P., 2022, in preparation

Munari E., Monaco P., Sefusatti E., Castorina E., Mohammad F. G., Anselmi S., Borgani S., 2017, *MNRAS*, **465**, 4658

Nunes R. C., Vagnozzi S., Kumar S., Di Valentino E., Mena O., 2022, *Phys. Rev. D*, **105**, 123506

Oddo A., Sefusatti E., Porciani C., Monaco P., Sánchez A. G., 2020, *J. Cosmology Astropart. Phys.*, **2020**, 056

Oddo A., Rizzo F., Sefusatti E., Porciani C., Monaco P., 2021, *J. Cosmology Astropart. Phys.*, **2021**, 038

Osato K., Nishimichi T., Bernardeau F., Taruya A., 2019, *Phys. Rev. D*, **99**, 063530

Paech K., Hamaus N., Hoyle B., Costanzi M., Giannantonio T., Hagstotz S., Sauerwein G., Weller J., 2017, *MNRAS*, **470**, 2566

Pan S., Yang W., Di Valentino E., Saridakis E. N., Chakraborty S., 2019, *Phys. Rev. D*, **100**, 103520

Perivolaropoulos L., Skara F., 2021, arXiv e-prints, p. [arXiv:2105.05208](https://arxiv.org/abs/2105.05208)

Perko A., Senatore L., Jennings E., Wechsler R. H., 2016, arXiv e-prints, p. [arXiv:1610.09321](https://arxiv.org/abs/1610.09321)

Philcox O. H. E., Ivanov M. M., 2022, *Phys. Rev. D*, **105**, 043517

Philcox O. H. E., Ivanov M. M., Cabass G., Simonović M., Zaldarriaga M., Nishimichi T., 2022, arXiv e-prints, p. [arXiv:2206.02800](https://arxiv.org/abs/2206.02800)

Planck Collaboration et al., 2020, *A&A*, **641**, A6

Pourtsidou A., Tram T., 2016, *Phys. Rev. D*, **94**, 043518

Pourtsidou A., Skordis C., Copeland E. J., 2013, *Phys. Rev. D*, **88**, 083505

Rizzo F., Moretti C., Pardede K., Eggemeier A., Oddo A., Sefusatti E., Porciani C., Monaco P., 2022, arXiv e-prints, p. [arXiv:2204.13628](https://arxiv.org/abs/2204.13628)

Sánchez A. G., et al., 2013, *MNRAS*, **433**, 1202

Scoccimarro R., Couchman H. M. P., Frieman J. A., 1999a, *ApJ*, **517**, 531

Scoccimarro R., Couchman H. M. P., Frieman J. A., 1999b, *ApJ*, **517**, 531

Seljak U., Hamaus N., Desjacques V., 2009, *Phys. Rev. Lett.*, **103**, 091303

Sellentin E., Heavens A. F., 2016, *MNRAS*, **456**, L132

Senatore L., Zaldarriaga M., 2014, arXiv e-prints, p. [arXiv:1409.1225](https://arxiv.org/abs/1409.1225)

Senatore L., Zaldarriaga M., 2015, *J. Cosmology Astropart. Phys.*, **2015**, 013

Simpson F., 2010, *Phys. Rev. D*, **82**, 083505

Skordis C., Pourtsidou A., Copeland E. J., 2015, *Phys. Rev. D*, **91**, 083537

Smith R. E., Scoccimarro R., Sheth R. K., 2007, *Phys. Rev. D*, **75**, 063512

Smith R. E., Sheth R. K., Scoccimarro R., 2008, *Phys. Rev. D*, **78**, 023523

Sotiriou T. P., Faraoni V., 2010, *Reviews of Modern Physics*, **82**, 451

Spergel D., et al., 2015, arXiv preprint arXiv:1503.03757

Spurio Mancini A., Pourtsidou A., 2022, *MNRAS*, **512**, L44

Tamanini N., 2015, *Phys. Rev. D*, **92**, 043524

Taruya A., Nishimichi T., Saito S., 2010, *Phys. Rev. D*, **82**, 063522

Tegmark M., 1997, *Phys. Rev. Lett.*, **79**, 3806

Väliviita J., Majerotto E., Maartens R., 2008, *J. Cosmology Astropart. Phys.*, **2008**, 020

Van Der Walt S., Colbert S. C., Varoquaux G., 2011, preprint, ([arXiv:1102.1523](https://arxiv.org/abs/1102.1523))

Van Rossum G., Drake Jr F. L., 1995, Python reference manual. Centrum voor Wiskunde en Informatica Amsterdam

Villaescusa-Navarro F., et al., 2020, *ApJS*, **250**, 2

Virtanen P., et al., 2020, *Nature Methods*, **17**, 261

Vlah Z., White M., 2019, *JCAP*, **03**, 007

Vlah Z., White M., Aviles A., 2015, *JCAP*, **09**, 014

Wang Y., 2008, *Phys. Rev. D*, **77**, 123525

Xia J.-Q., 2009, *Phys. Rev. D*, **80**, 103514

Yang W., Pan S., Saló L. A., de Haro J., 2021, *Phys. Rev. D*, **103**, 083520

Yankelevich V., Porciani C., 2019, *MNRAS*, **483**, 2078

d'Amico G., Gleyzes J., Kokron N., Markovic K., Senatore L., Zhang P., Beutler F., Gil-Marín H., 2020, *J. Cosmology Astropart. Phys.*, **2020**, 005

van de Bruck C., Thomas C. C., 2019, *Phys. Rev. D*, **100**, 023515

**APPENDIX A: FULL POSTERIOR DISTRIBUTIONS**

We collect here the full posterior distributions for the different runs described in the text.

This paper has been typeset from a  $\text{\TeX}/\text{\LaTeX}$  file prepared by the author.

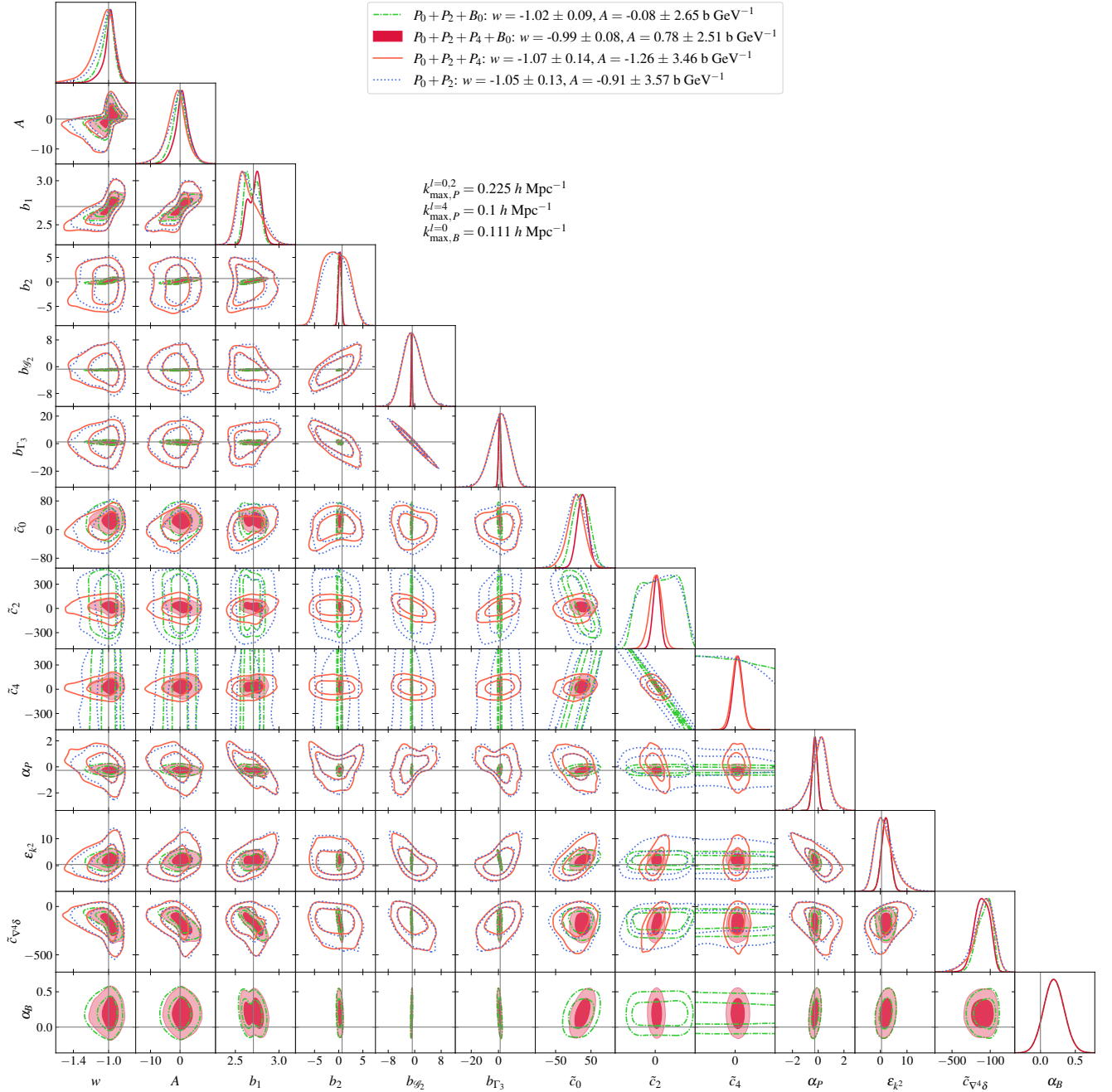


**Figure A1.** Posterior distributions for the base model with the scale cuts given in the triangle plot. The power spectrum monopole and quadrupole analysis is denoted by the dotted blue line, constraints from all power spectrum multipoles are given by the solid orange line, joint analysis of power spectrum monopole plus quadrupole and bispectrum monopole is presented by the dotted-dashed light-green line, and the full joint analysis is shown by the dark-red contours. Thin grey lines correspond to the fiducial values known from the fiducial cosmology and previous analysis of this data set in [Oddo et al. \(2020, 2021\)](#); [Rizzo et al. \(2022\)](#).

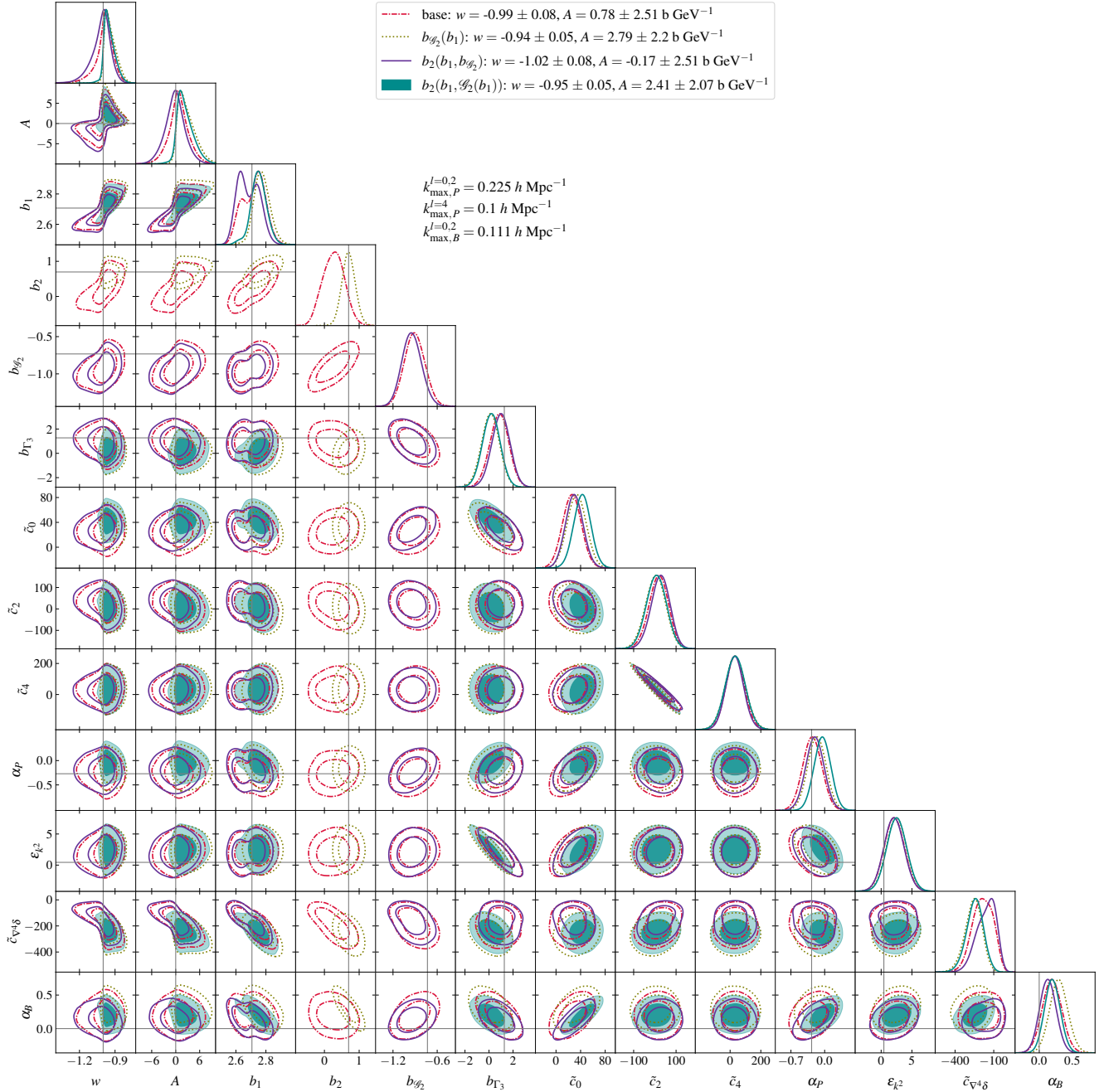


**Figure A2.** Posterior distributions for the  $P_0 + P_2 + P_4 + B_0$  models with bias relations at the scale cuts given on the triangle plot. The joint analysis with the base model is shown by the dark-red dotted-dashed lines, olive dotted lines denote the tidal bias relation, purple solid lines represent the  $b_2$ -relation, the dark-cyan contours denote the combined relation of  $b_2$  and  $b_{\mathcal{G}_2}$ . Thin grey lines correspond to the fiducial values known from the fiducial cosmology and previous analysis of this data set in [Oddo et al. \(2020, 2021\)](#); [Rizzo et al. \(2022\)](#).

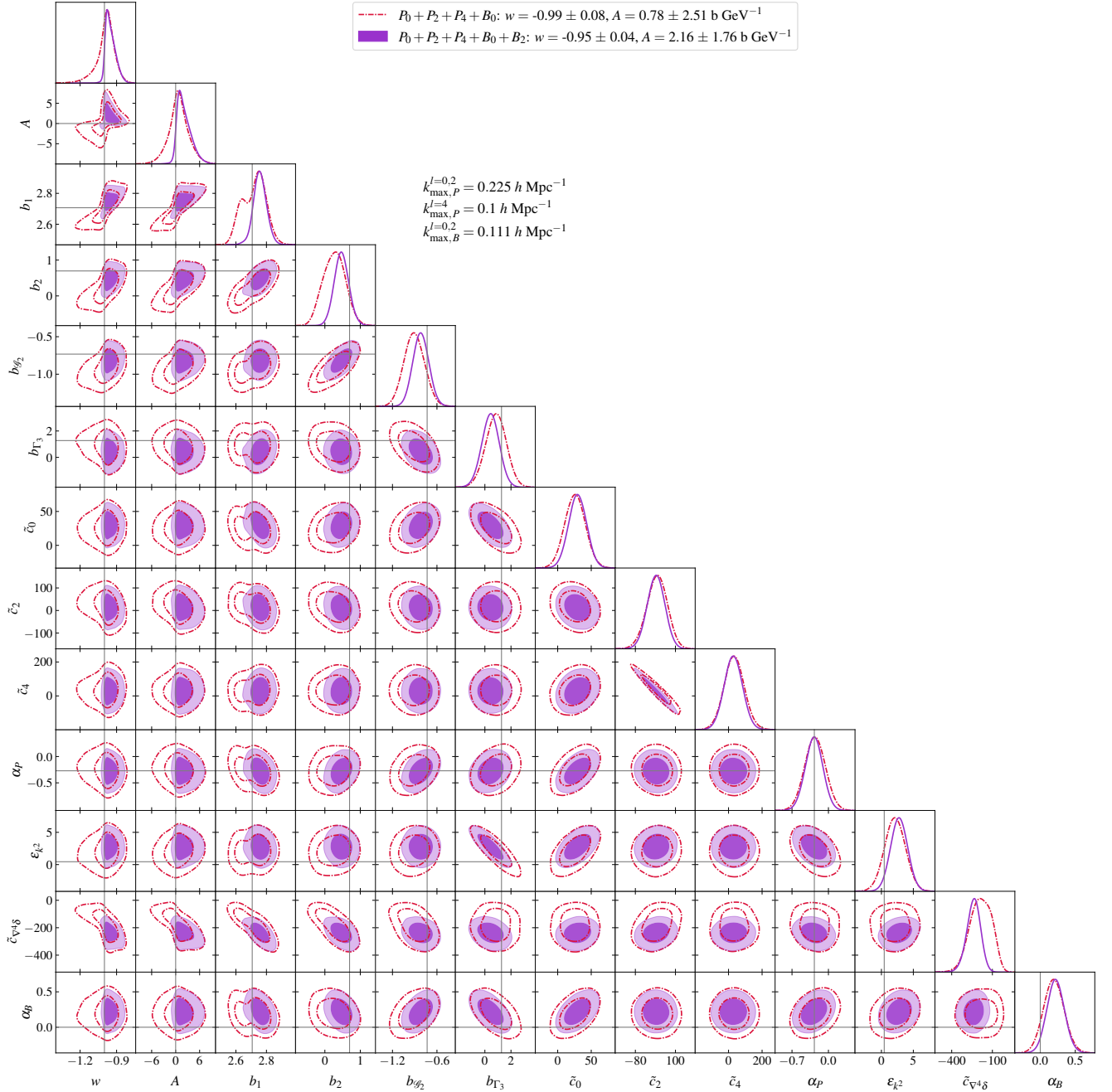


**Figure A3.** Posterior distributions for the base model with and without the bispectrum quadrupole at the scale cuts given on the triangle plot. The joint analysis with the bispectrum monopole is shown by the dark-red dotted-dashed lines, the joint analysis with the bispectrum monopole and quadrupole is denoted by the purple contours. Thin grey lines correspond to the fiducial values known from the fiducial cosmology and previous analysis of this data set in [Oddo et al. \(2020, 2021\)](#); [Rizzo et al. \(2022\)](#).

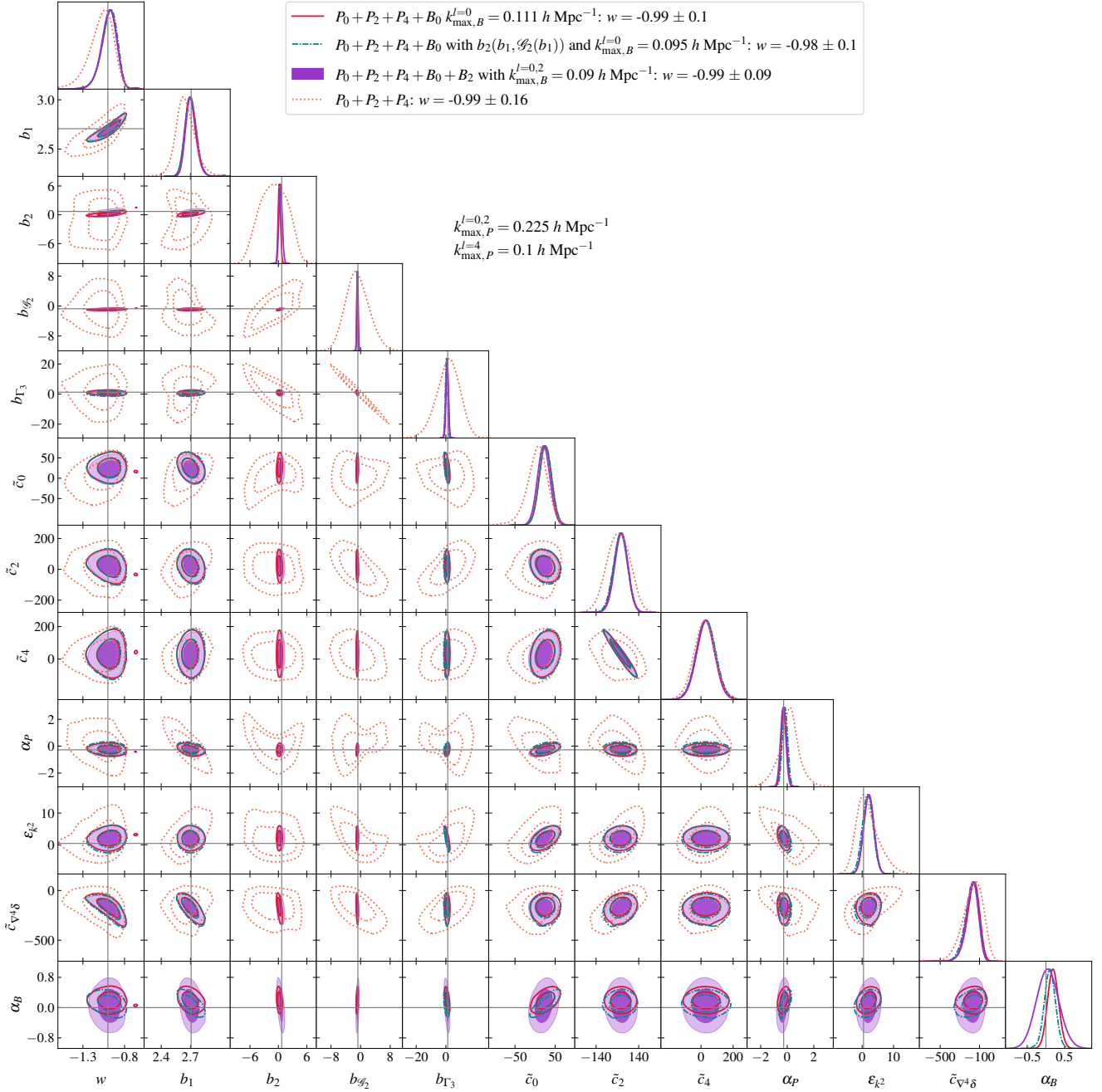


**Figure A4.** Posterior distributions for the  $w$ CDM model for four models at the scale cuts given on the triangle plot. The joint analysis with the bispectrum monopole is shown by the solid dark-red lines, the joint analysis with the bispectrum monopole with the combined bias relation is given by the dotted-dashed dark-cyan lines, the joint analysis with the bispectrum monopole and quadrupole is denoted by the purple contours, constraints from all power spectrum multipoles are shown by the dotted orange line. Thin grey lines correspond to the fiducial values known from the fiducial cosmology and previous analysis of this data set in [Oddo et al. \(2020, 2021\)](#); [Rizzo et al. \(2022\)](#).